

## **General Disclaimer**

### **One or more of the Following Statements may affect this Document**

- This document has been reproduced from the best copy furnished by the organizational source. It is being released in the interest of making available as much information as possible.
- This document may contain data, which exceeds the sheet parameters. It was furnished in this condition by the organizational source and is the best copy available.
- This document may contain tone-on-tone or color graphs, charts and/or pictures, which have been reproduced in black and white.
- This document is paginated as submitted by the original source.
- Portions of this document are not fully legible due to the historical nature of some of the material. However, it is the best reproduction available from the original submission.

(NASA-CR-175704) VARIATIONAL MESOSCALE  
SATELLITE DATA ASSIMILATION AND  
INITIALIZATION Final Report, 15 Jan. 1983 -  
31 Dec. 1984 (Oklahoma Univ.) 73 p  
HC A04/MF A01

N85-24680

Unclas  
CSCI 04B G3/47 22308

FINAL REPORT

for

NATIONAL AERONAUTICS AND SPACE ADMINISTRATION  
Research Grant No. NAG 5-289  
(1/15/83 to 12/31/84)

VARIATIONAL MESOSCALE SATELLITE DATA  
ASSIMILATION AND INITIALIZATION

submitted by

Yoshi K. Sasaki, Principal Investigator  
George Lynn Cross Research Professor  
School of Meteorology, University of Oklahoma

and

Director, Cooperative Institute for Mesoscale Meteorological Studies

and

James S. Goerss, Co-principal Investigator  
Research Scientist  
Cooperative Institute for Mesoscale Meteorological Studies

Norman, Oklahoma

May, 1985

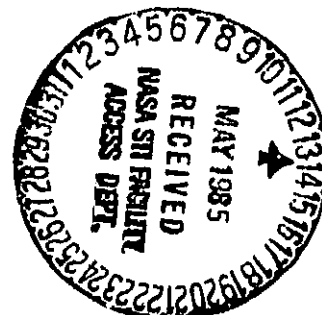


## TABLE OF CONTENTS

	PAGE
1. INTRODUCTION.....	1
2. DATA ASSESSMENT.....	3
3. VARIATIONAL TEMPERATURE ANALYSIS.....	23
4. MESOSCALE MODEL.....	32
5. ASSIMILATION EXPERIMENT	
Initialization Procedures.....	43
Model Forecasts.....	47
6. CONCLUSIONS AND RECOMMENDATIONS.....	68
BIBLIOGRAPHY.....	71

## 1. INTRODUCTION

Over the past several years we have conducted many experiments in the area of global satellite data assimilation. Most of these experiments have dealt with the assimilation of satellite-derived temperature data either continuously or intermittently into a global primitive equations model. We have found that when properly performed, satellite data assimilation has a positive impact upon the global model forecasts. Using the experience we have gained from our global satellite data assimilation experiments, we have turned our attention to the problems of mesoscale satellite data assimilation. Our overall research goal is to utilize the assimilation of satellite data in order to improve the forecasts made by mesoscale forecast models.

Specifically, the problem we report on here has dealt with the assimilation of high resolution ( $\sim 30$  km) satellite-derived temperature data into a mesoscale model with horizontal resolution of 50-60 km. Unlike global assimilation, in which a small portion of the forecast model domain is subject to data insertion at virtually every time step, mesoscale assimilation is such that virtually all of the forecast model domain is subject to data insertion at one time step. Thus, the mesoscale problem lends itself naturally to intermittent data assimilation and the forecast model is re-initialized whenever a new satellite pass covers its domain with data. In this research we have treated the satellite data assimilation as an initialization problem.

In the next section we discuss the satellite and conventional data sets available for use in this study. The variational temperature analysis scheme we have developed to combine the temperature information contained in these two types of observations is described and demonstrated in Section 3. The

CIMMS Mesoscale Model is the forecast model which we used in this study to assess the impact of the satellite data assimilation. It evolved from the global primitive equations model we have used in our global assimilation work. A description of the model is given in Section 4. Finally, in Section 5 we discuss the results of the forecast experiments which culminated our research efforts. Three different initialization procedures are compared with and without satellite data assimilation.

## 2. DATA ASSESSMENT

### Satellite Data

The satellite data which were available for this study were brightness temperatures from one orbit for the TIROS-N High Resolution Infrared Radiation Sounder (HIRS) and Microwave Sounder Unit (MSU) channels as determined by NESS at the University of Wisconsin. The TIROS-N orbit was for 15 January 1979 at 0850 GMT and covered roughly the eastern half of the United States. The resolution of the satellite data was on the order of about 30 km.

In Fig. 1, it can be seen that at 12 GMT, 15 January 1979 a large high pressure system was centered on the eastern U.S. As a result, most of this area was relatively cloud-free as indicated by the nephanalysis displayed in Fig. 2. The density of the TIROS-N observations is compared to that for the FGGE Level II-b surface observations in Fig. 3. The satellite observations shown in this figure are those from areas that have been determined to be relatively cloud-free. In this study we are interested in utilizing the information about horizontal temperature gradients contained in the TIROS-N brightness temperatures. From Fig. 3 we can see that one can expect gradients to be more sharply defined by the higher resolution satellite observations than the surface observations. The upper air observational network has even lower resolution than the surface network.

We next examined the brightness temperatures for the various HIRS and MSU channels. Plots of this variable for HIRS Channel 13 and MSU Channel 3 are shown in Figs. 4 and 5. The brightness temperature for HIRS Channel 13 can be thought of as roughly a mean layer temperature for a layer extending from the

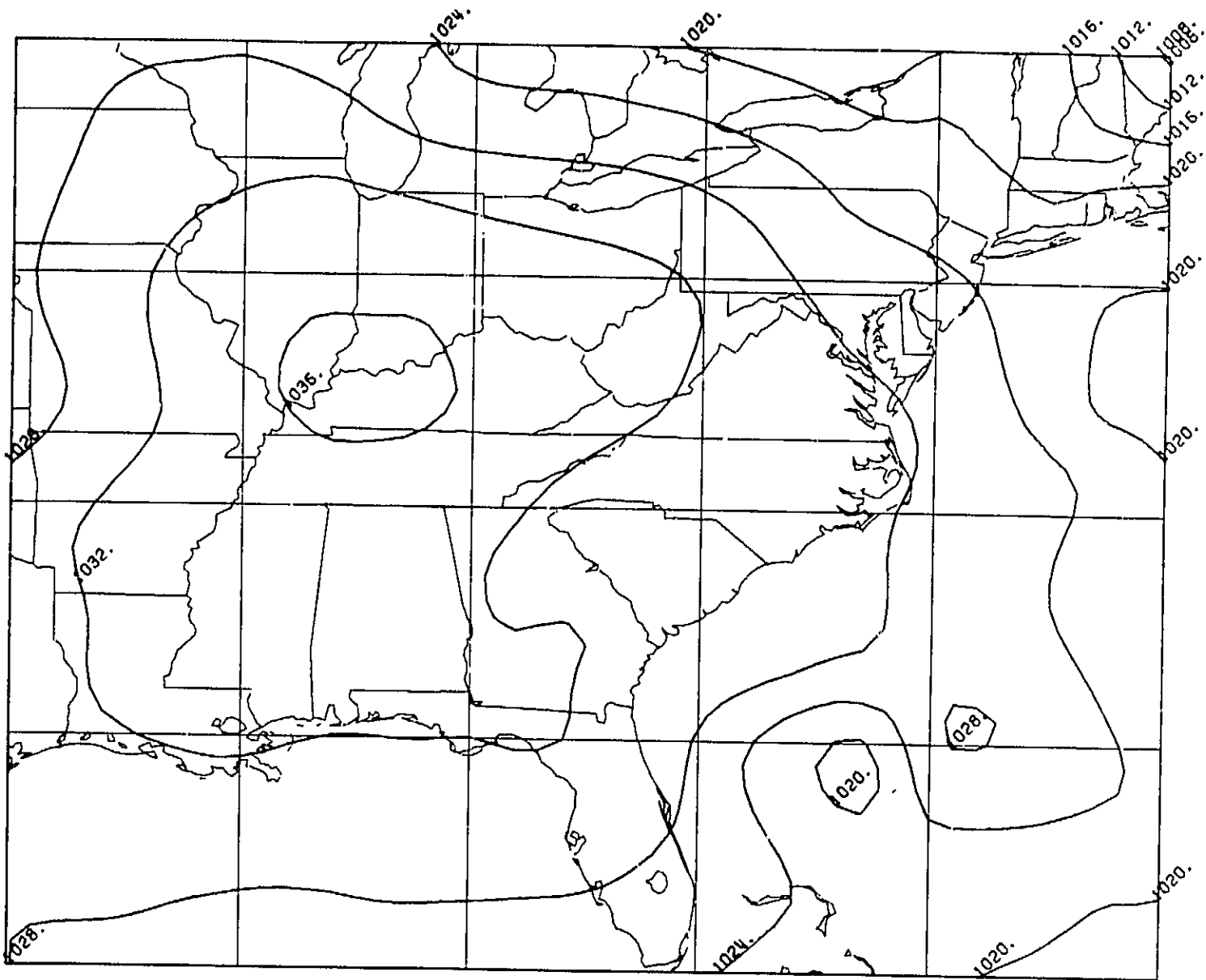


Fig. 1. Sea-level pressure analysis for 12 GMT, 15 January 1979.

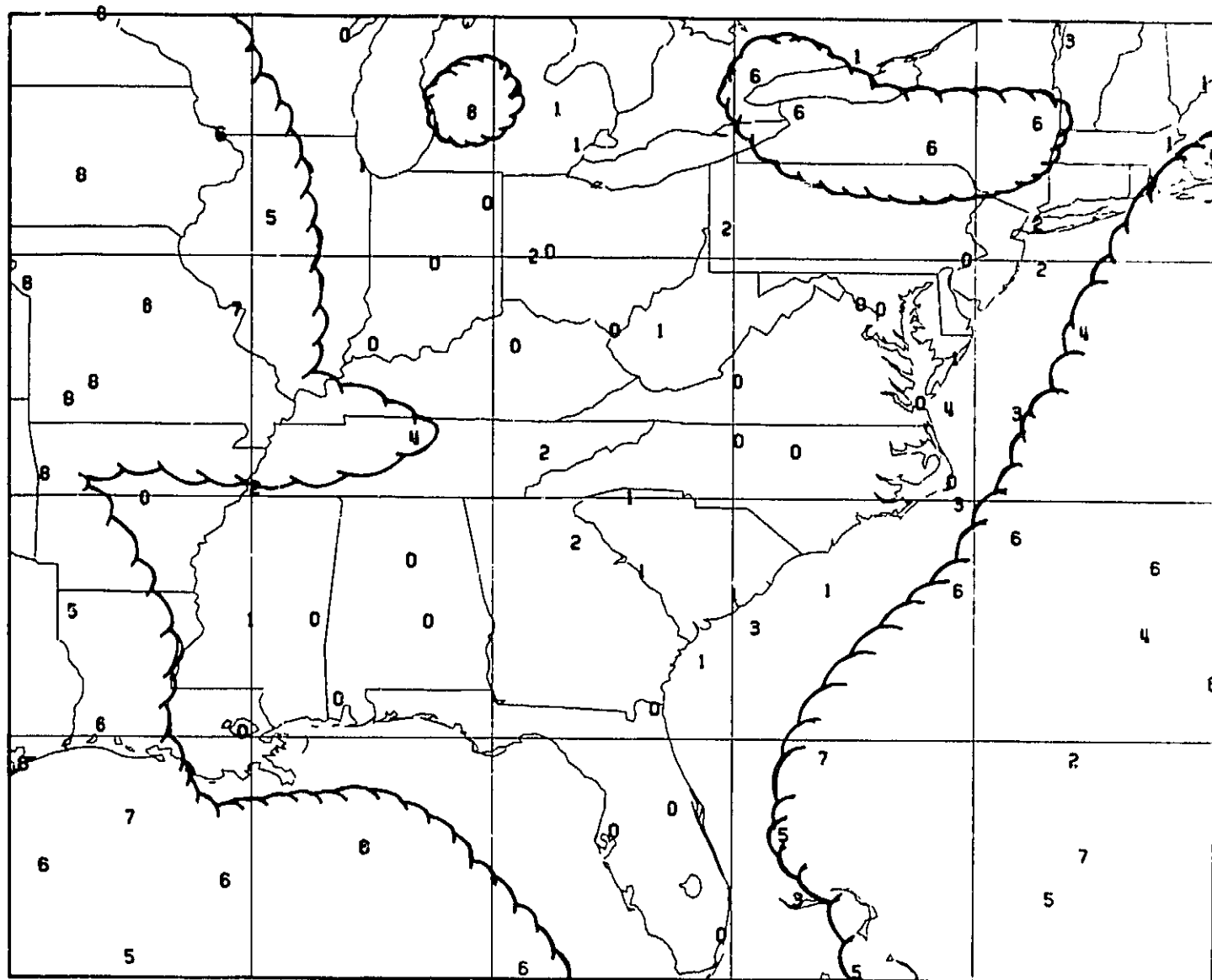
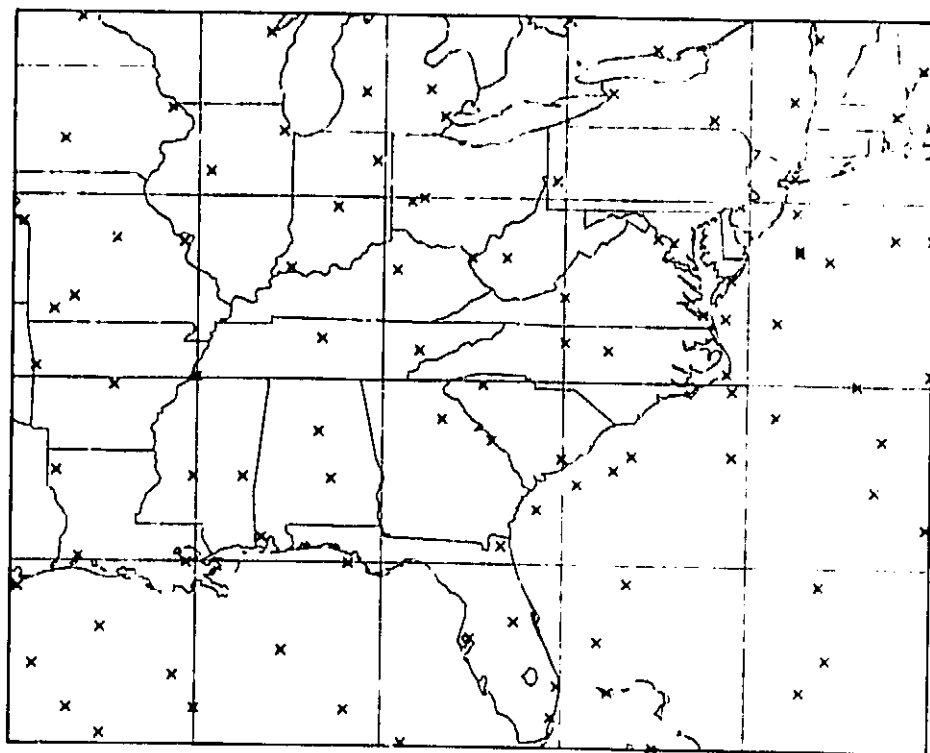


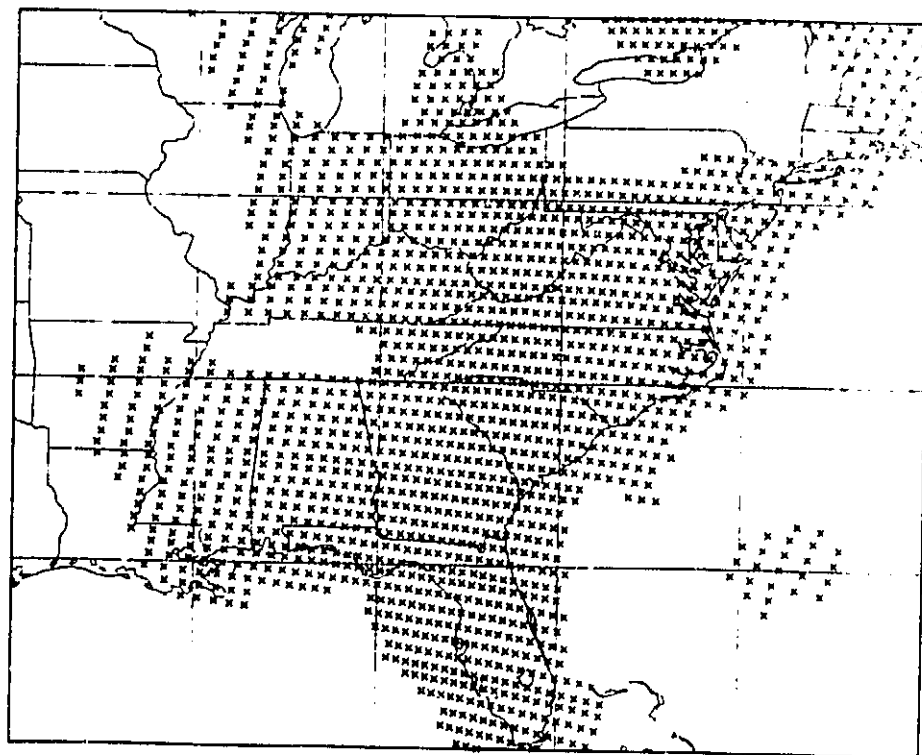
Fig. 2. Observed sky cover and nephanalysis from surface observations for 12 GMT, 15 January 1979.





Surface Obs, 12Z, 15 Jan 1979

ORIGINAL PAGE IS  
OF POOR QUALITY



TIROS-N Obs, 09Z, 15 Jan 1979

Fig. 3 Surface and satellite observational density.

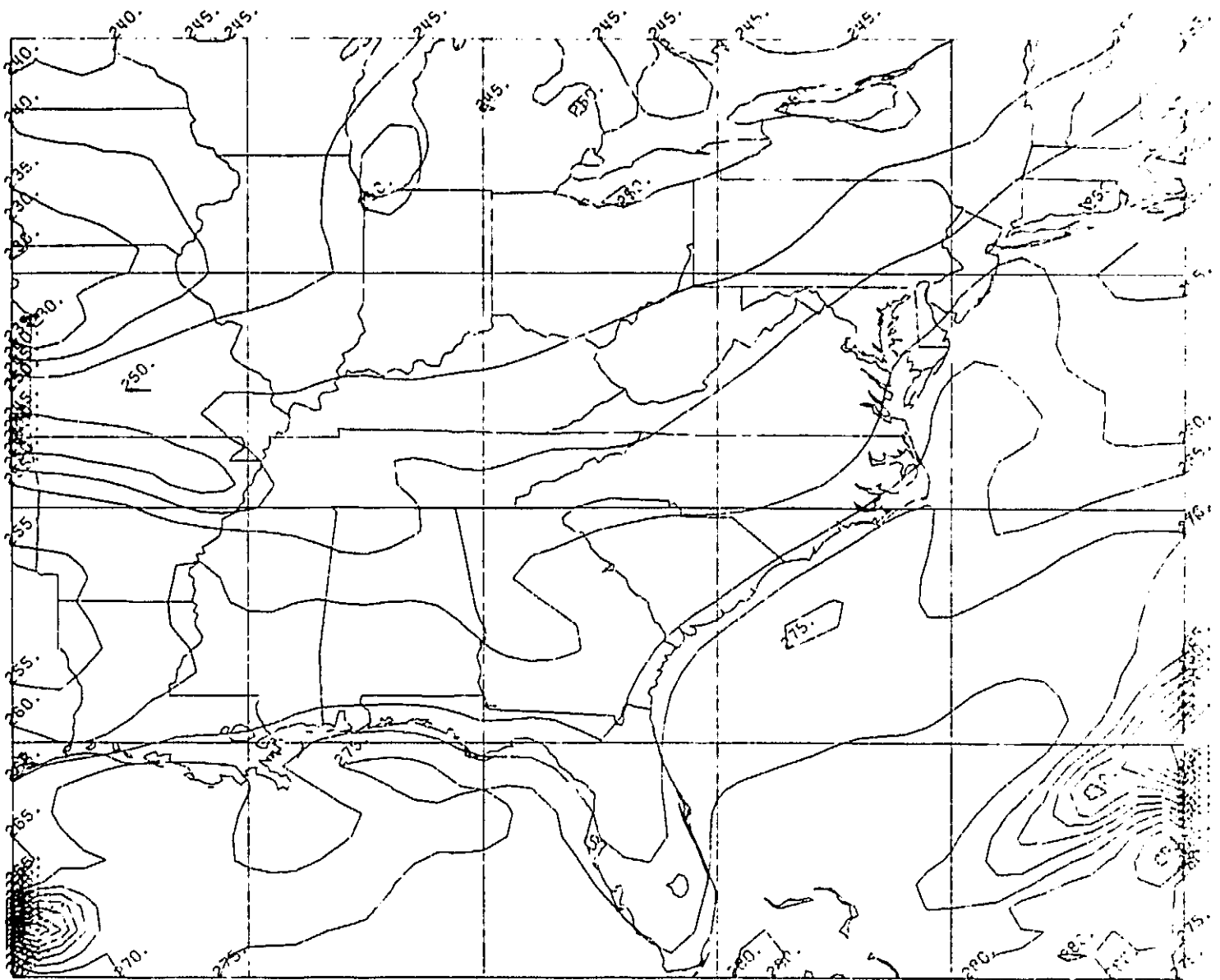


Fig. 4 HIRS Channel 13 brightness temperatures.

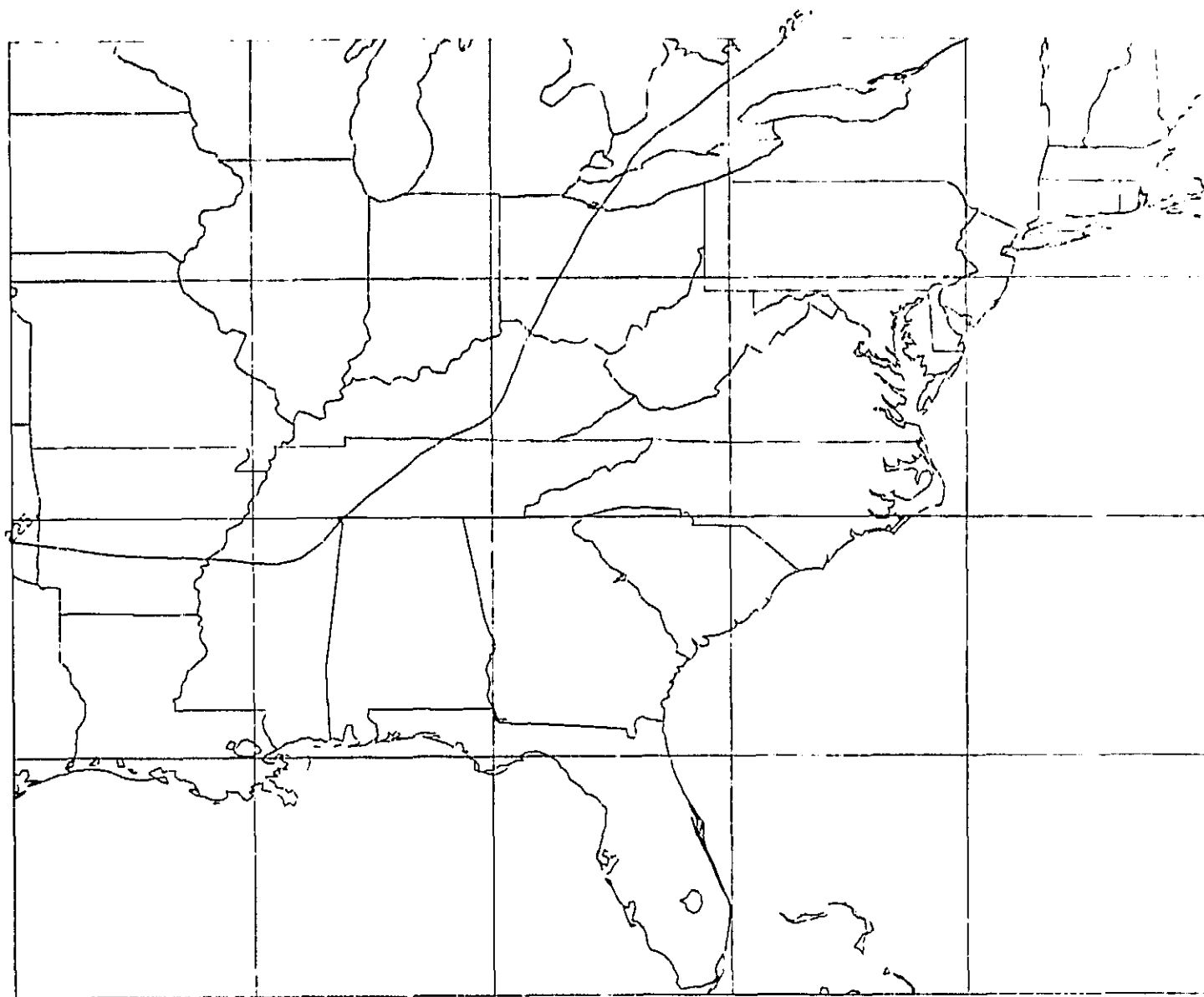


Fig. 5 MSU Channel 3 brightness temperatures.

surface to about 800 mb while that for MSU Channel 3 represents the mean layer temperature for a layer extending from about 600 mb to 100 mb. These inferences are based upon the weighting functions for these channels shown in Fig. 6. In the cloud-free areas we can see in Fig. 4 that temperature gradient structure is evident while in Fig. 5 we see that there is virtually no temperature gradient whatsoever. This can be understood by examining the weighting function for MSU Channel 3 and the FGGE Level III-b temperature fields valid at 12 GMT, 15 January, at 500 mb, 300 mb, and 150 mb displayed in Figs. 7-9. In Fig. 7 we see that there is a definite north-south temperature gradient with cold air to the north at 500 mb. This gradient is still apparent at 300 mb though not as strong (Fig. 8), but at 150 mb we see in Fig. 9 that the temperature gradient has reversed itself with warm air to the northeast and cold air to the southwest. The broad weighting function for MSU Channel 3 indicates that the resulting brightness temperatures will represent an average for a deep layer. The horizontal temperature gradients at the top of this layer are almost the reverse of those at the bottom of the layer. Thus, the resulting average is a field with virtually no horizontal temperature gradient. Therefore, we concluded that the TIROS-N brightness temperatures themselves were of most use for the very lowest layers of the atmosphere where the weighting functions for the appropriate channels peak more sharply.

#### **FGGE Level II-b and III-b Data**

In this study we had available both FGGE Level II-b and III-b data for the time period of interest. The FGGE Level II-b data set is the Global Experiment Research Data Set, which is distinguished from the operational II-a

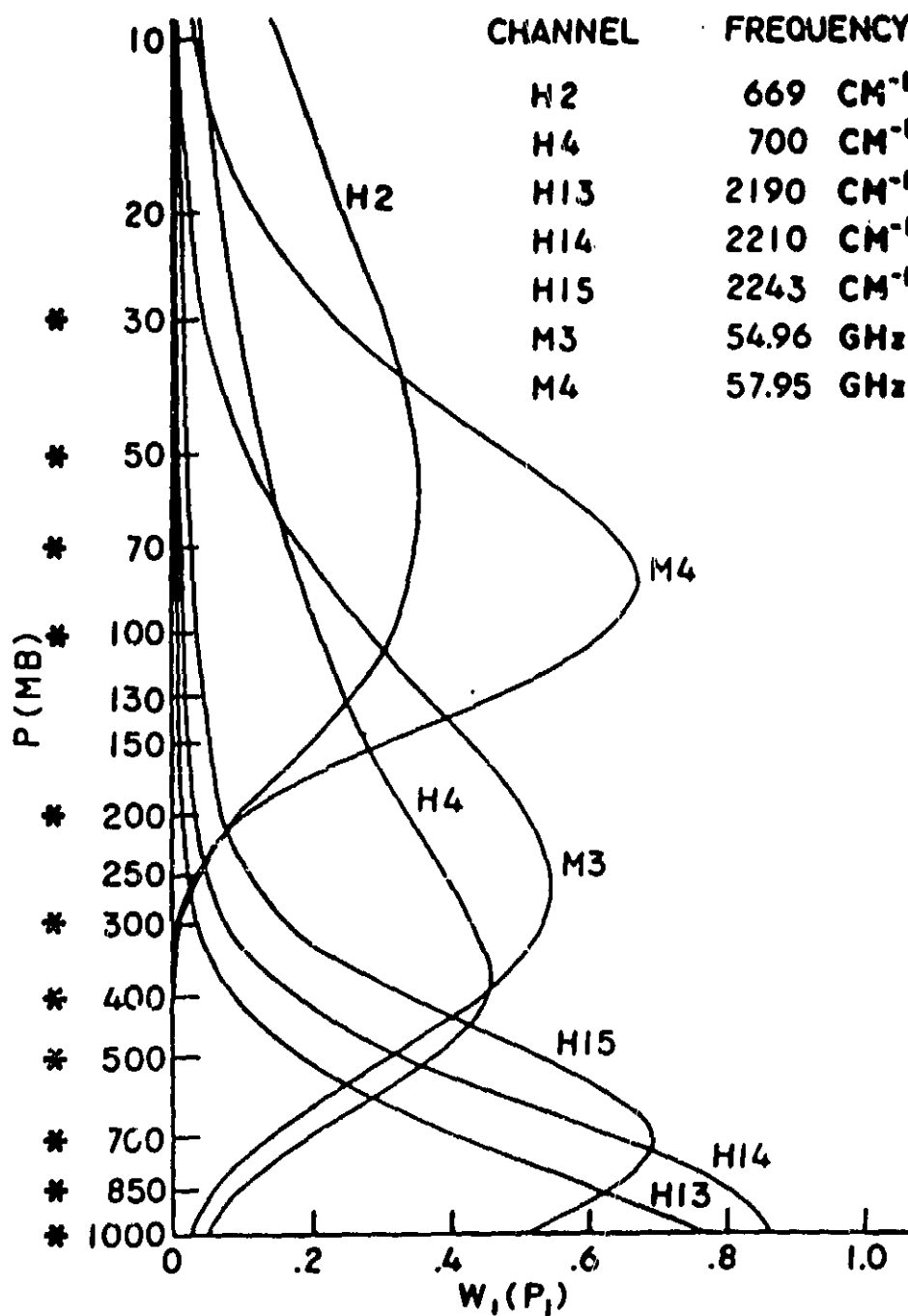


Fig. 6 Weighting functions, for U.S. standard atmosphere at nadir viewing, for seven HIRS2-MSU channels. (from Susskind, et al., 1982)

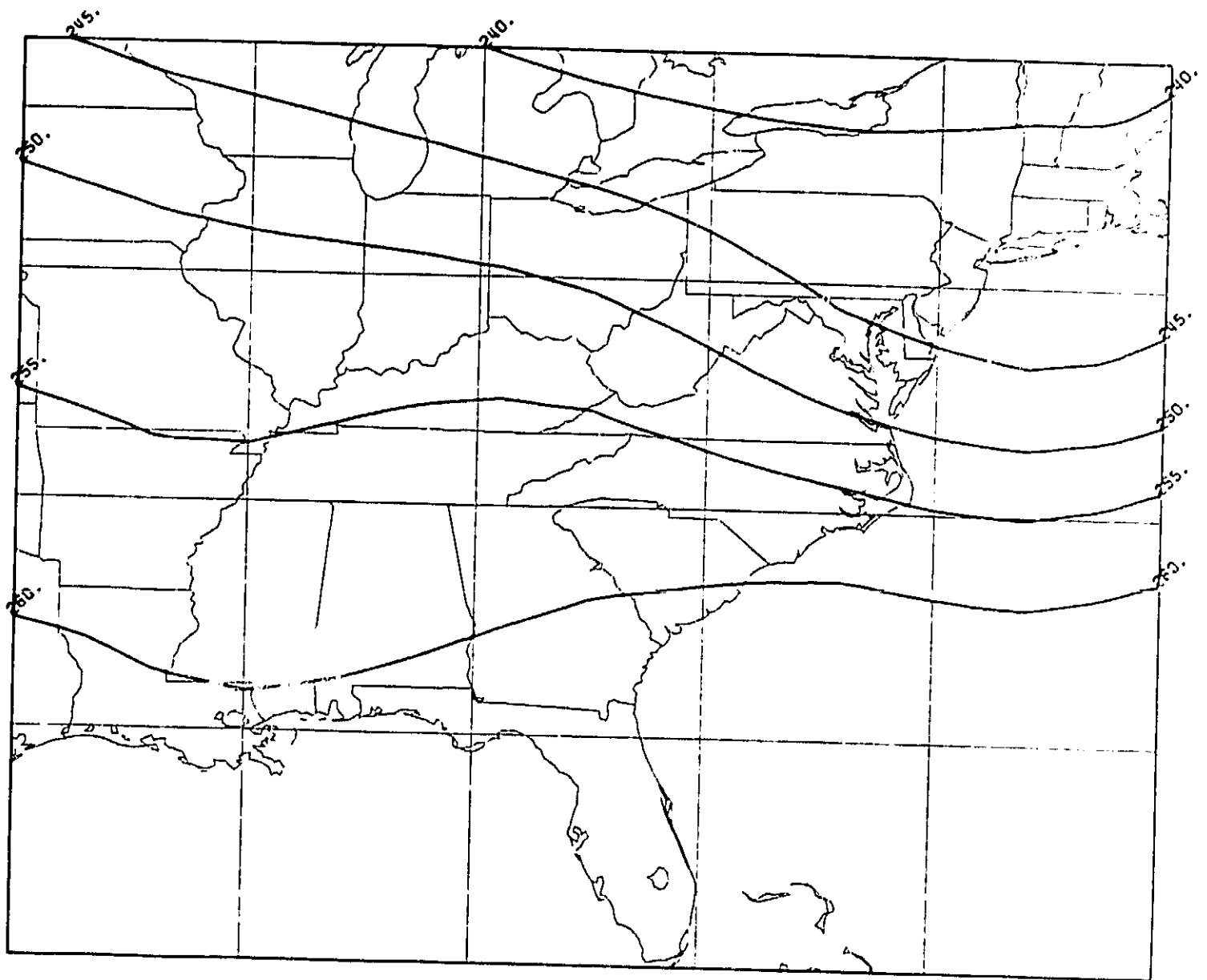


Fig. 7 FGGE Level III-b 500 mb temperature field, 12 GMT, 15 January 1979.

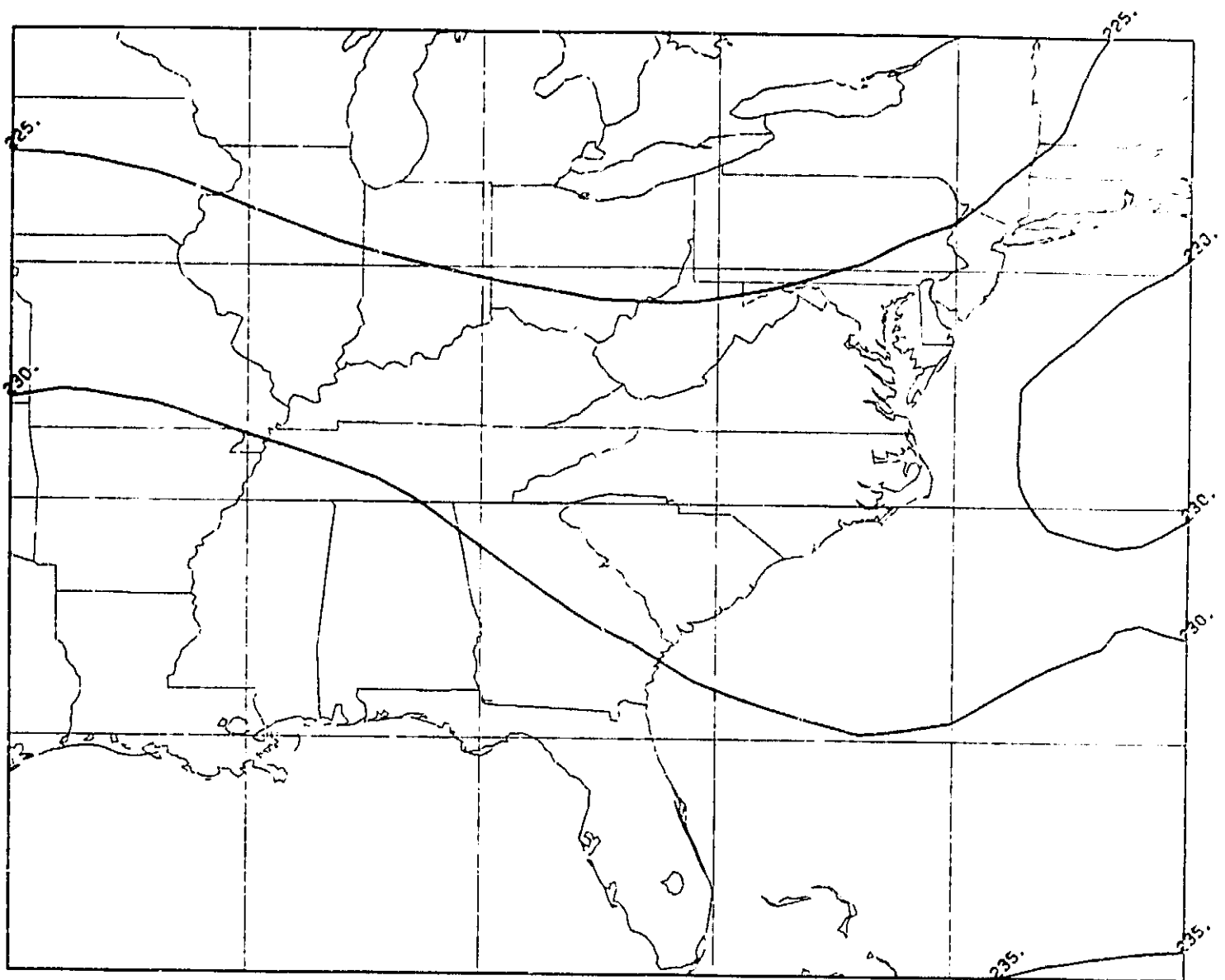


Fig. 8 FGGE Level III-b 300 mb temperature field, 12 GMT, 15 January 1979.

ORIGINAL FILED IN  
OF POOR QUALITY

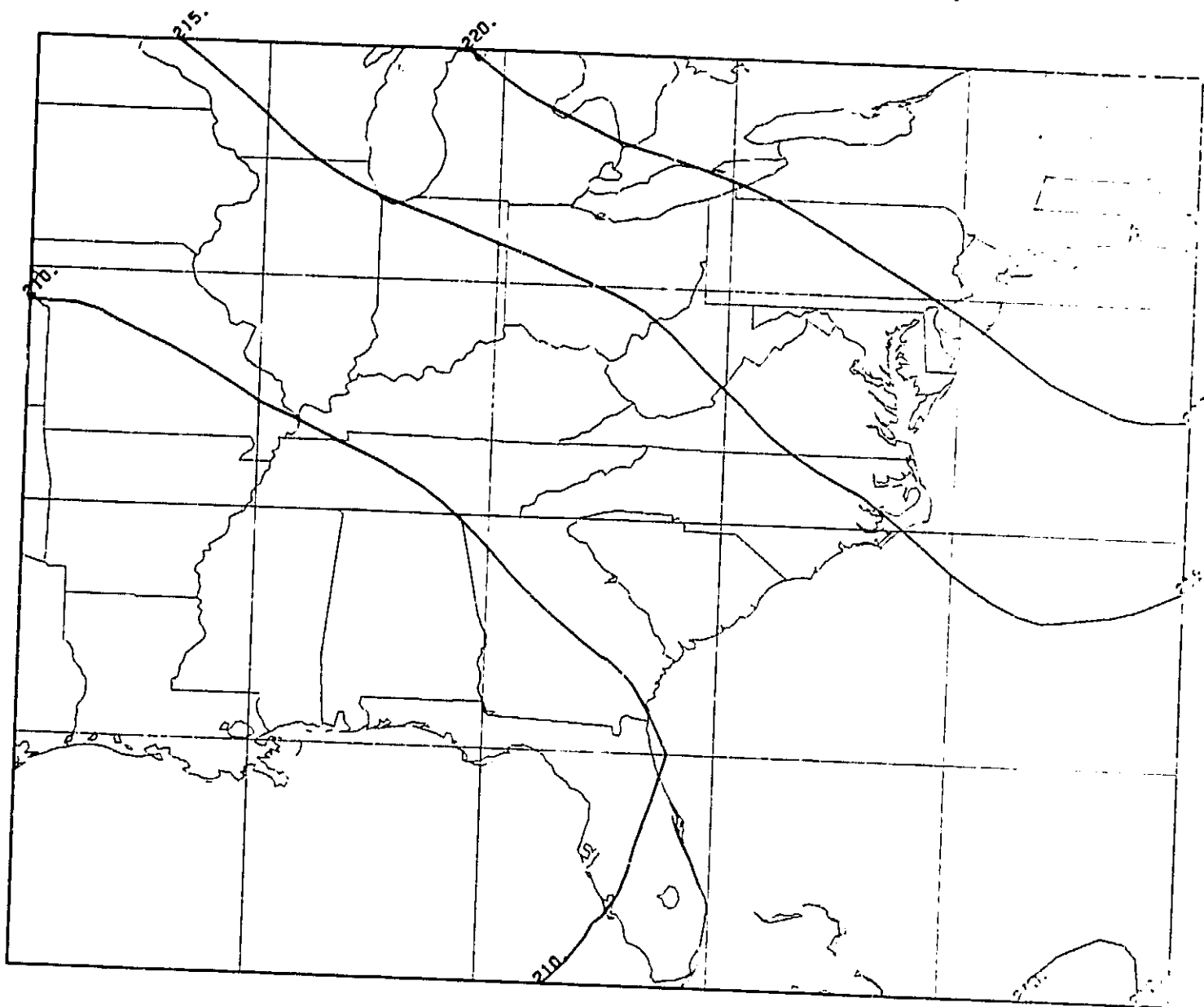
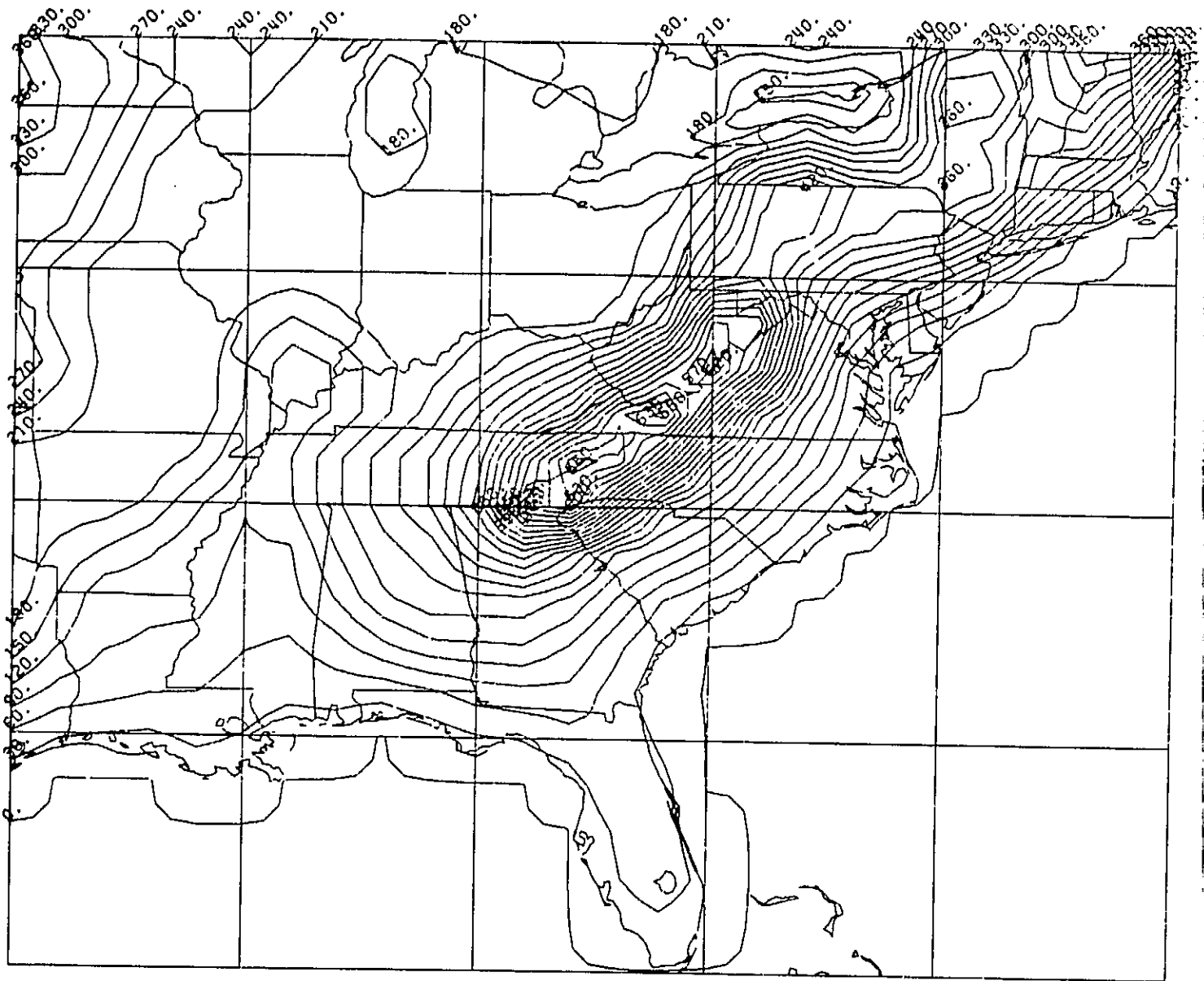


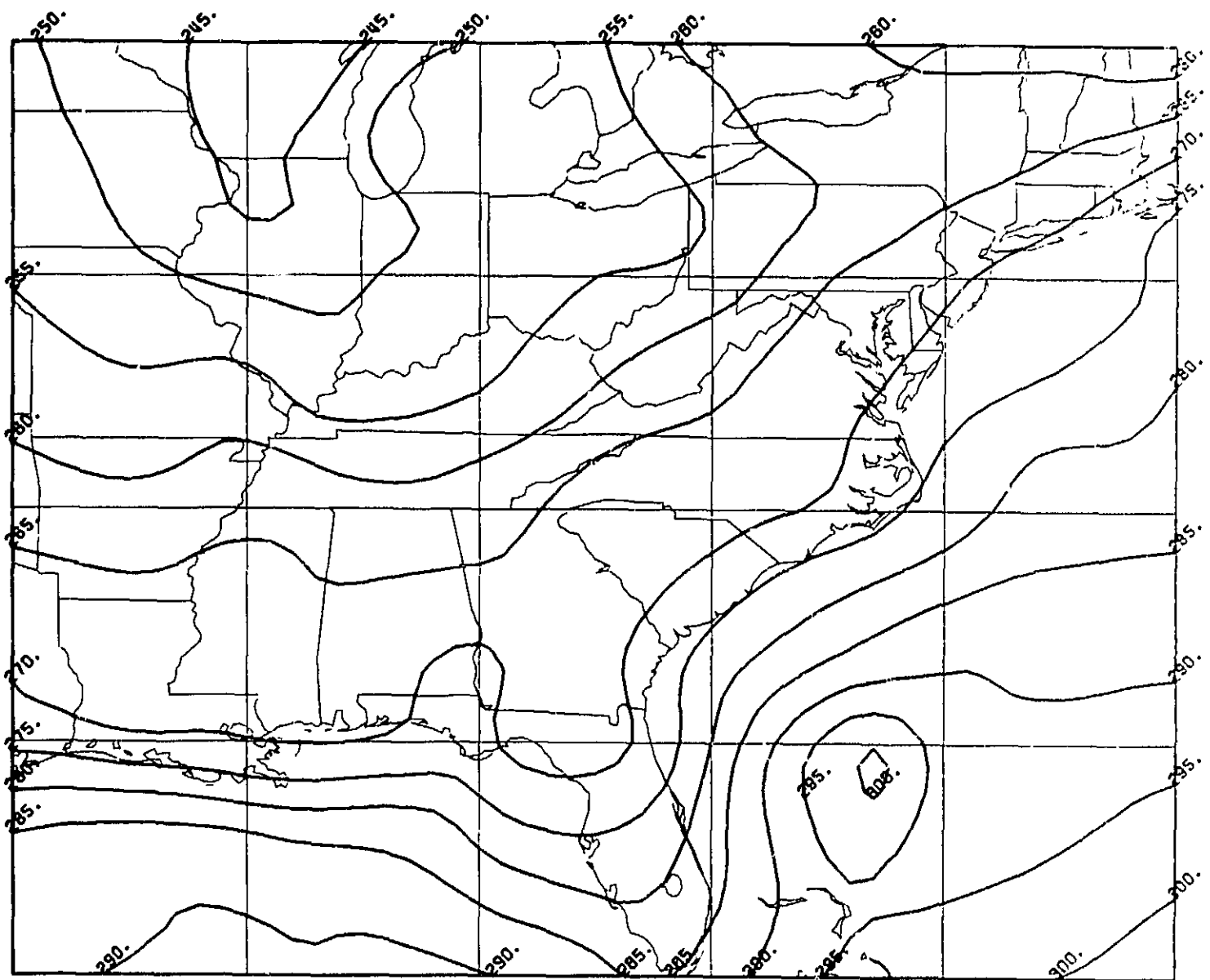
Fig. 9 FGGE Level III-b 150 mb temperature field, 12 GMT, 15 January 1979.



data set by a delayed cutoff to acquire a complete global data set. This data set contains the majority of all routine weather observations globally observed and transmitted over the Global Telecommunications System in 6-hour cycles. These data are augmented on a massive scale with observations from many special systems: satellites, aircraft, buoys, ships, and balloons during the FGGE Special Observing Periods. The FGGE Level III-b data set consists of analyses produced by the European Centre for Medium Range Weather Forecasts operational system using the Level II-b rather than II-a data sets as input.

Using the FGGE Level II-b and III-b data sets from 12 GMT, 15 January 1979, we analyzed temperature at the surface as well as at the standard pressure levels (1000 mb, 850 mb, 700 mb, etc.). Heights and temperatures at the standard pressure levels were obtained from the FGGE Level III-b data, and using the terrain heights illustrated in Fig. 10, a surface temperature field was produced by interpolation to a  $0.5^\circ$  grid for the domain illustrated. This surface temperature field was then used as the first-guess field for a Cressman analysis of the Level II-b surface temperature observations. The resulting temperature analysis is shown in Fig. 11. The radii of influence for the Cressman analysis were chosen to reflect the resolution of the surface observations as shown in Fig. 3. We can see from this temperature analysis that the strongest temperature gradients are found along the coastal areas of the Gulf of Mexico and the southeast Atlantic seaboard. The definition of these surface temperature gradients is limited by the resolution of the surface observations. Using the FGGE Level III-b temperature fields as first-guess fields, Cressman analyses of the Level II-b upper air observations were performed for the standard pressure levels. The radii of influence for these





Contour interval  
OF 5.0

Fig. 11 Cressman analysis of FGGE Level II-b surface temperature observations, 12 GMT, 15 January 1979.

analyses were chosen to reflect the resolution of the upper air data. Figs. 12 and 13 display the resulting analyses for 700 mb and 200 mb.

In view of our examination of the satellite data we concluded that it would only be feasible to produce temperature analyses enhanced by TIROS-N brightness temperatures in the very lowest layers of the atmosphere. Using the analyzed surface temperature field shown in Fig. 11 as a first-guess field, the brightness temperatures from HIRS Channel 8 (the 11  $\mu$ m longwave window) were analyzed. Only the brightness temperatures from areas determined to be relatively cloud-free were used (see Fig. 3). The resulting Cressman analysis, whose radii of influence reflected the high resolution of the satellite observations, is shown in Fig. 14. The most striking difference between this satellite-derived surface temperature analysis and the conventional analysis shown in Fig. 11 is the enhanced temperature gradients in the coastal areas. These gradients are much more sharply defined in both their horizontal structure as well as their intensity. This is graphically illustrated in Fig. 15 where the difference field between these two analyzed fields is shown.

In order to better understand the differences between these two surface temperature analyses, each was compared with the actual surface temperature observations. The bias and rmse were computed for the differences between the surface observations and the values of each field interpolated to the locations of the observations. For the conventional analysis the bias and rmse were -0.01K and 1.04K, respectively. The respective values for the satellite-derived analysis were -1.58K and 3.76K. Since the first field is merely a Cressman analysis of the surface observations themselves, we expect that the values for the bias and rmse will be quite small, and indeed they are. The

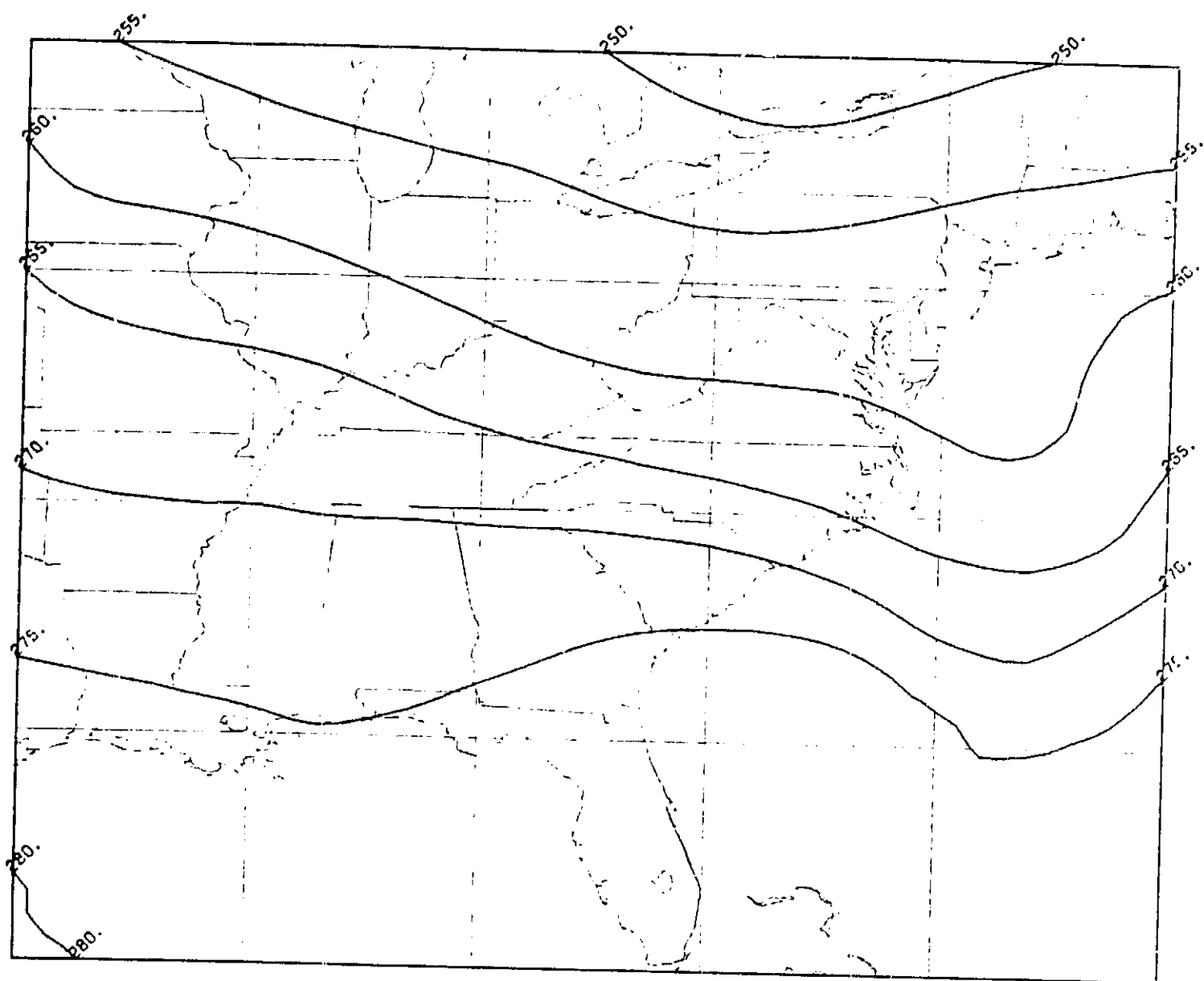


Fig. 12 Cressman analysis of FGGE Level II-b upper air 700 mb temperature observations 12 GMT, 15 January 1979.

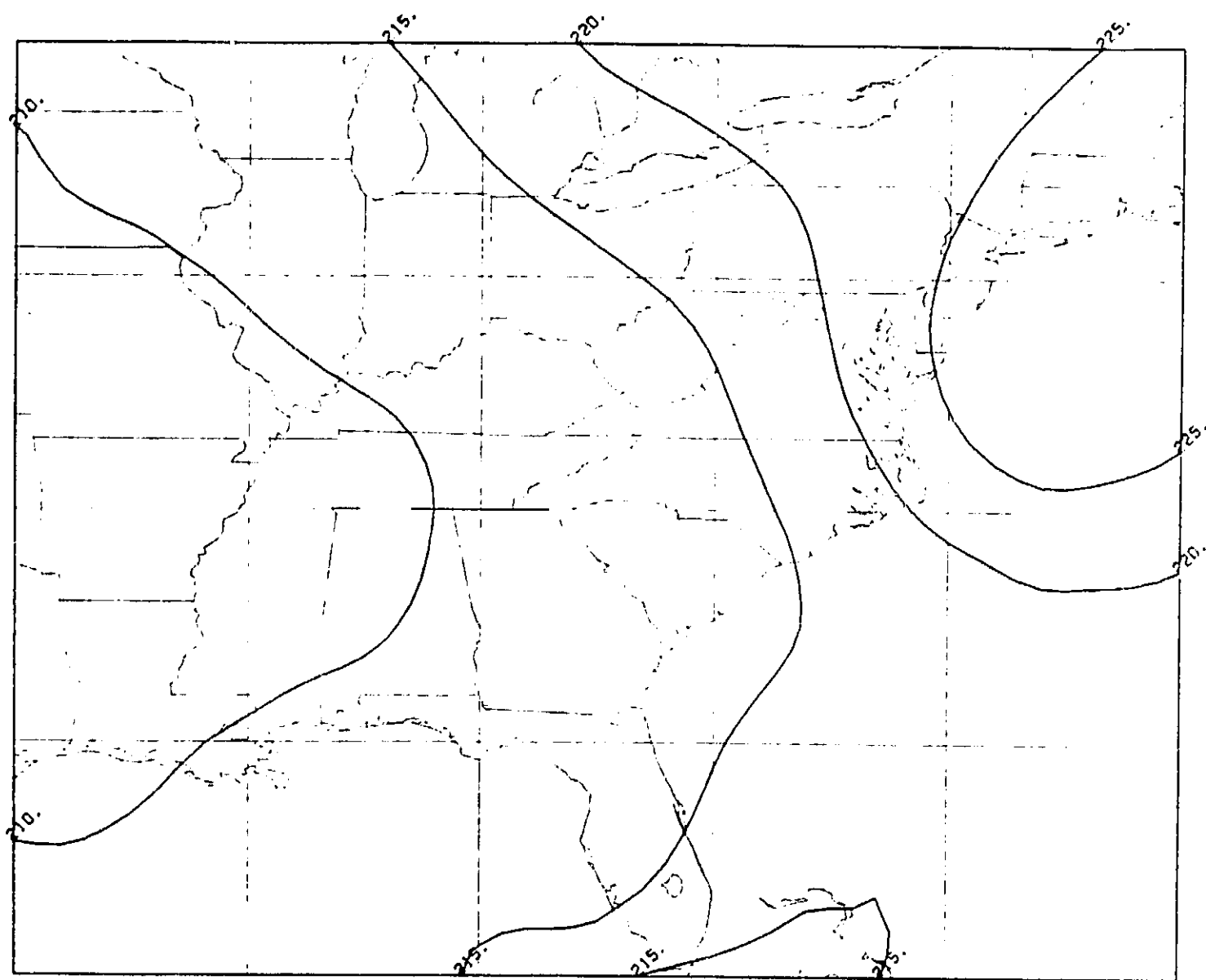


Fig. 13 Cressman analysis of FGGE Level II-b upper air 200 mb temperature observations, 12 GMT, 15 January 1979.

ORIGINAL  
OF POOR QUALITY

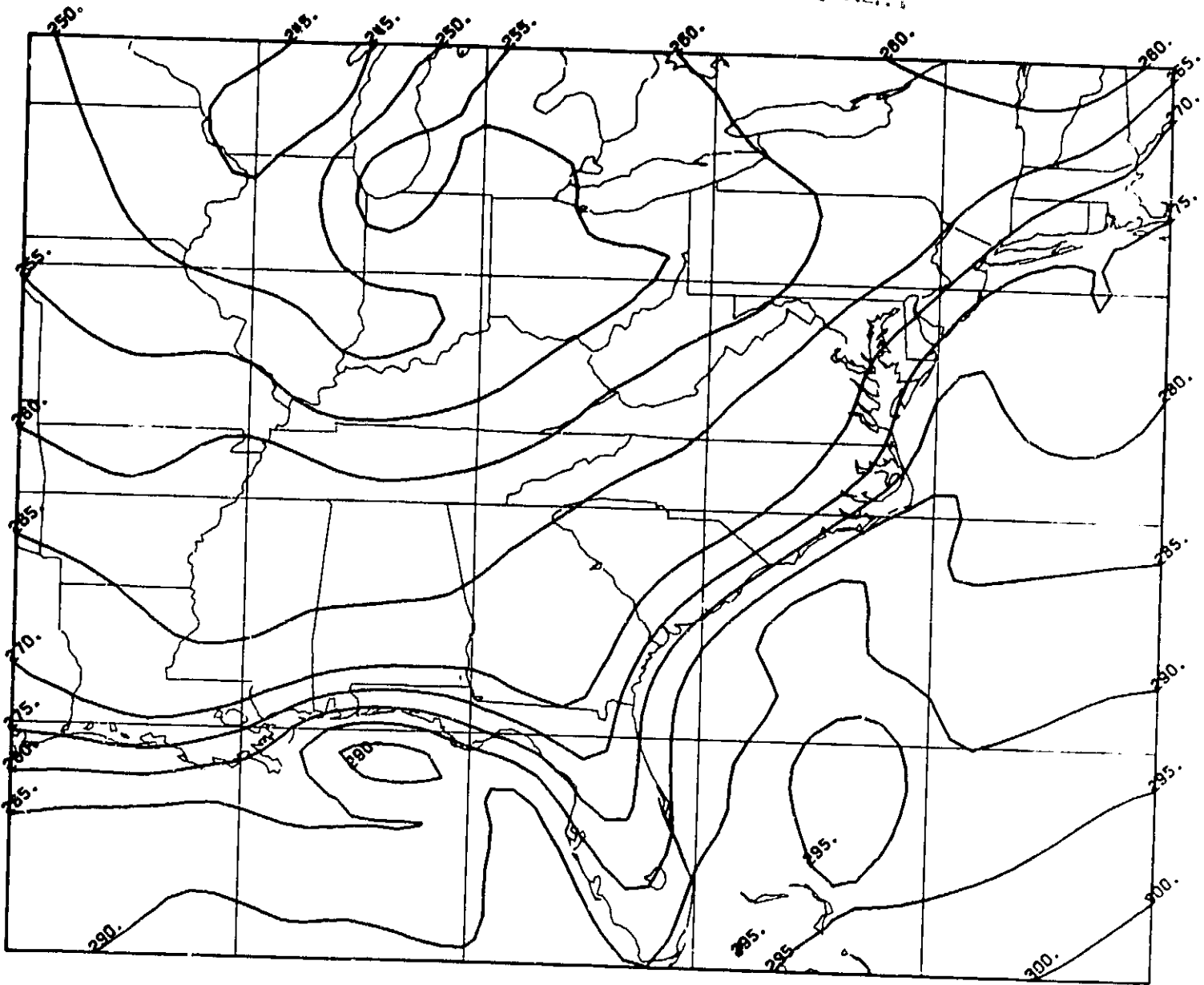


Fig. 14 Cressman analysis of HIRS Channel 8 brightness temperature, 12 GMT, 15 January 1979.

CHART  
OF POOR QUALITY

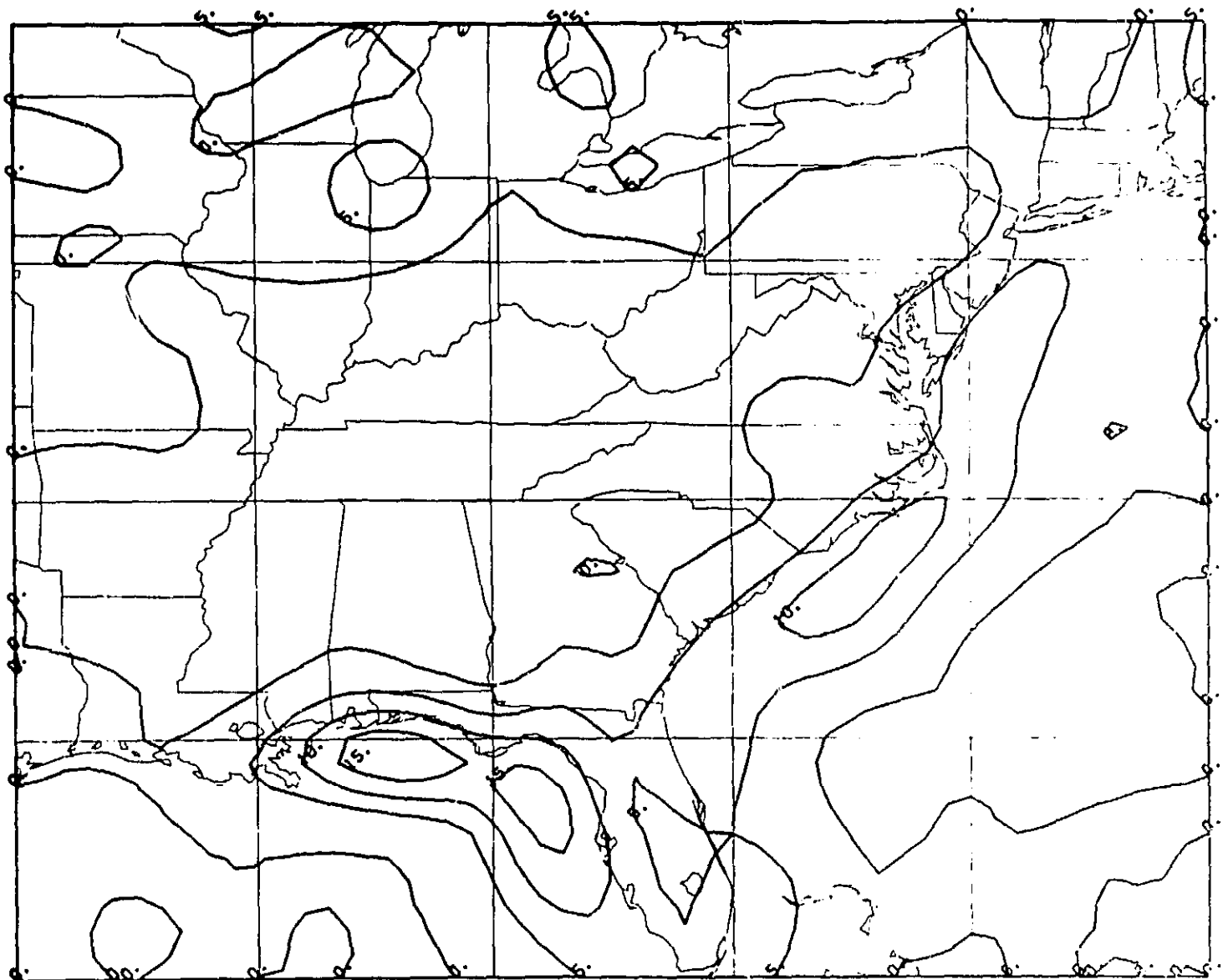


Fig. 15      Difference field between analyzed temperature fields for 12 GMT, 15 January 1979 (Fig. 14 minus Fig. 11).



satellite-derived field displays a large bias with respect to the surface observations along with a larger rmse. However, the high resolution temperature gradient information contained in this field is potentially valuable. In the next section we describe a variational analysis scheme designed to combine the useful information contained in the conventional and satellite-derived surface temperature fields.

### 3. VARIATIONAL TEMPERATURE ANALYSIS

The philosophy behind the variational temperature analysis scheme is to combine horizontal temperature gradient information derived at high resolution from satellite with absolute temperature information derived from conventional observations and/or a model forecast. The analysis is obtained by minimizing the functional  $J$  in spherical coordinates:

$$J = \int_{\theta_1}^{\theta_2} \int_{\lambda_1}^{\lambda_2} \{ A(T - \tilde{T})^2 + B(\nabla_{\lambda} T - \nabla_{\lambda} \hat{T})^2 + C(\nabla_{\theta} T - \nabla_{\theta} \hat{T})^2 + D(\nabla_{\lambda}^2 T - \nabla_{\lambda}^2 \hat{T})^2 + E(\nabla_{\theta}^2 T - \nabla_{\theta}^2 \hat{T})^2 \} d\lambda d\theta \quad (1)$$

where  $T$  is the analyzed temperature,  $\tilde{T}$  is the absolute temperature, and  $\hat{T}$  is a satellite-derived temperature. The gradients and Laplacians are separated into their longitudinal ( $\lambda$ ) and latitudinal ( $\theta$ ) components.  $A$ ,  $B$ ,  $C$ ,  $D$ , and  $E$  are data weights whose values are chosen to be roughly equal to the inverse of the expected variance of their associated differences in (1). The units of these weights are such that each term in (1) is dimensionless. In order to satisfy the boundary conditions when the variation of  $J$  is taken, the weights are set to zero as appropriate. This functional can be evaluated on any surface and is readily solved by relaxation.

In order to test the analysis scheme we use it to combine the surface temperature field derived using conventional observations displayed in Fig. 11 with the field shown in Fig. 14 derived using high-resolution satellite observations. The conventionally analyzed temperatures are denoted by  $\tilde{T}$  and the satellite-derived temperatures by  $\hat{T}$  in functional  $J$ . The variational

temperature analysis is to be performed upon a 41 x 51 grid with 0.5° resolution extending from 25 N to 45 N and from 95 W to 70 W.

By varying the relative values of the weights in (1), we can control the influence of the  $\tilde{T}$ - and  $\hat{T}$ -fields upon the analysis resulting from minimizing the functional J. Three cases will be shown here. In each case the value of A is taken to be 0.1. In the first case  $B = C = 1.E9$  and  $D = E = 1.E18$ . The resulting temperature analysis ( $T_1$ ) is shown in Fig. 16 and the difference field ( $T_1 - \tilde{T}$ ) in Fig. 17. Table 1 summarizes some statistics computed for the three cases ( $T_1$ ,  $T_2$ , and  $T_3$ ) as well as for the  $\tilde{T}$ - and  $\hat{T}$ -fields. In the first case the relative weighting upon the satellite temperature gradient and Laplacian information is weak and the analysis field agrees more with the surface observations. Cases 2 and 3 are shown in Figs. 18-21 and represent medium and strong weighting of the satellite temperature information, respectively. In Case 2,  $B = C = 3.E9$  and  $D = E = 3.E18$

Table 1. RMSE's between various temperature fields and observations of temperature and horizontal derivatives of temperature.

Field	Surface Obs. (K)	$\nabla \hat{T} (K m^{-1})$	$\nabla^2 \hat{T} (K m^{-2})$
$\tilde{T}$	1.04	2.7E-5	4.1E-10
$\hat{T}$	3.76	0	0
$T_1$	1.70	1.2E-5	1.3E-10
$T_2$	2.23	7.1E-6	6.0E-11
$T_3$	2.70	3.6E-6	2.5E-11

while in Case 3,  $B = C = 1.E10$  and  $D = E = 1.E19$ . From the RMSE's in Table 1 we can see that as the relative strength of the weighting upon the satellite

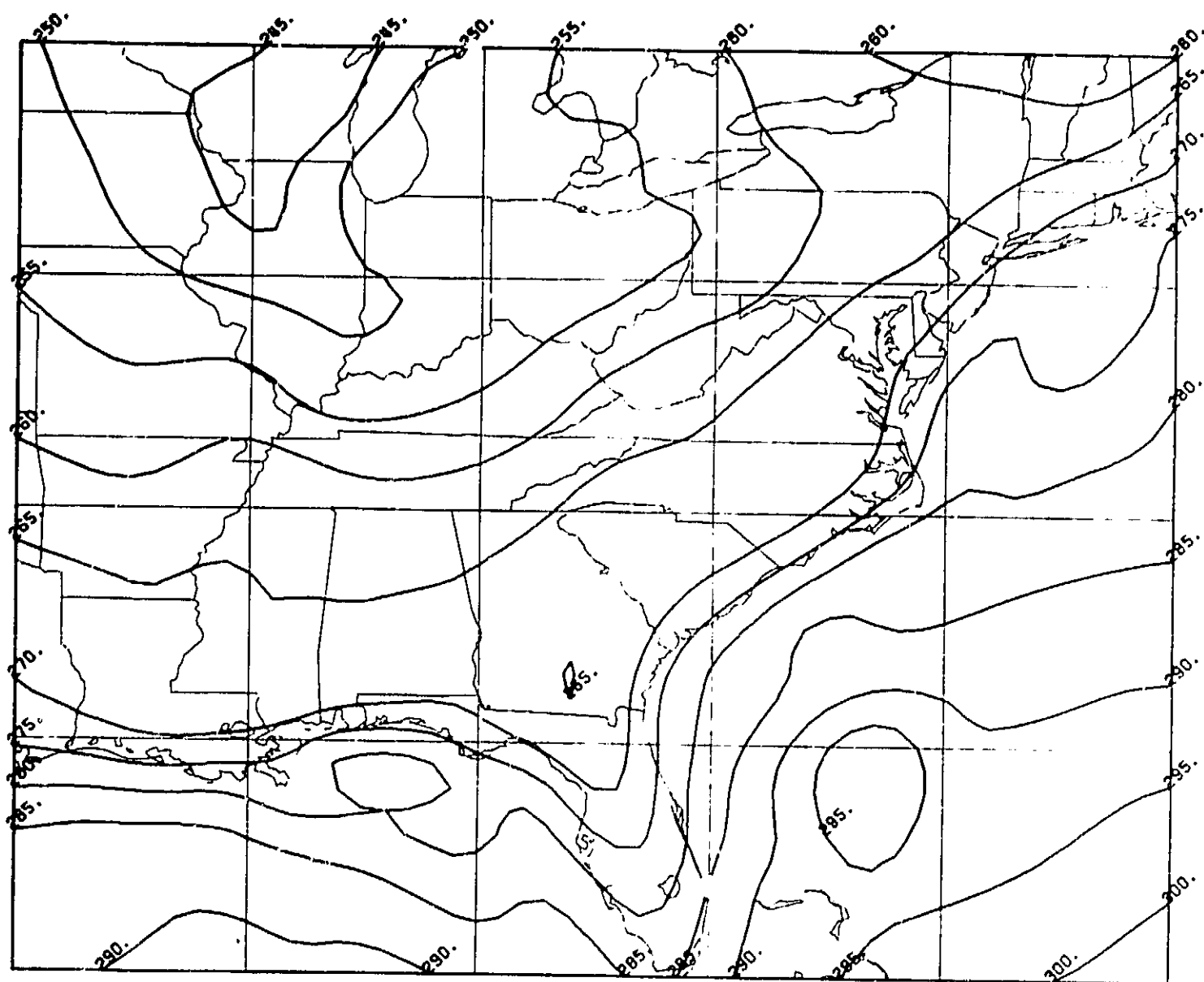


Fig. 16 Variational temperature analysis ( $T_1$ ) for 12 GMT, 15 January 1979  
( $A = 0.1$ ,  $B = C = 1.E9$ ,  $D = E = 1.E18$ ).

ORIGINAL MAP  
OF POOR QUALITY

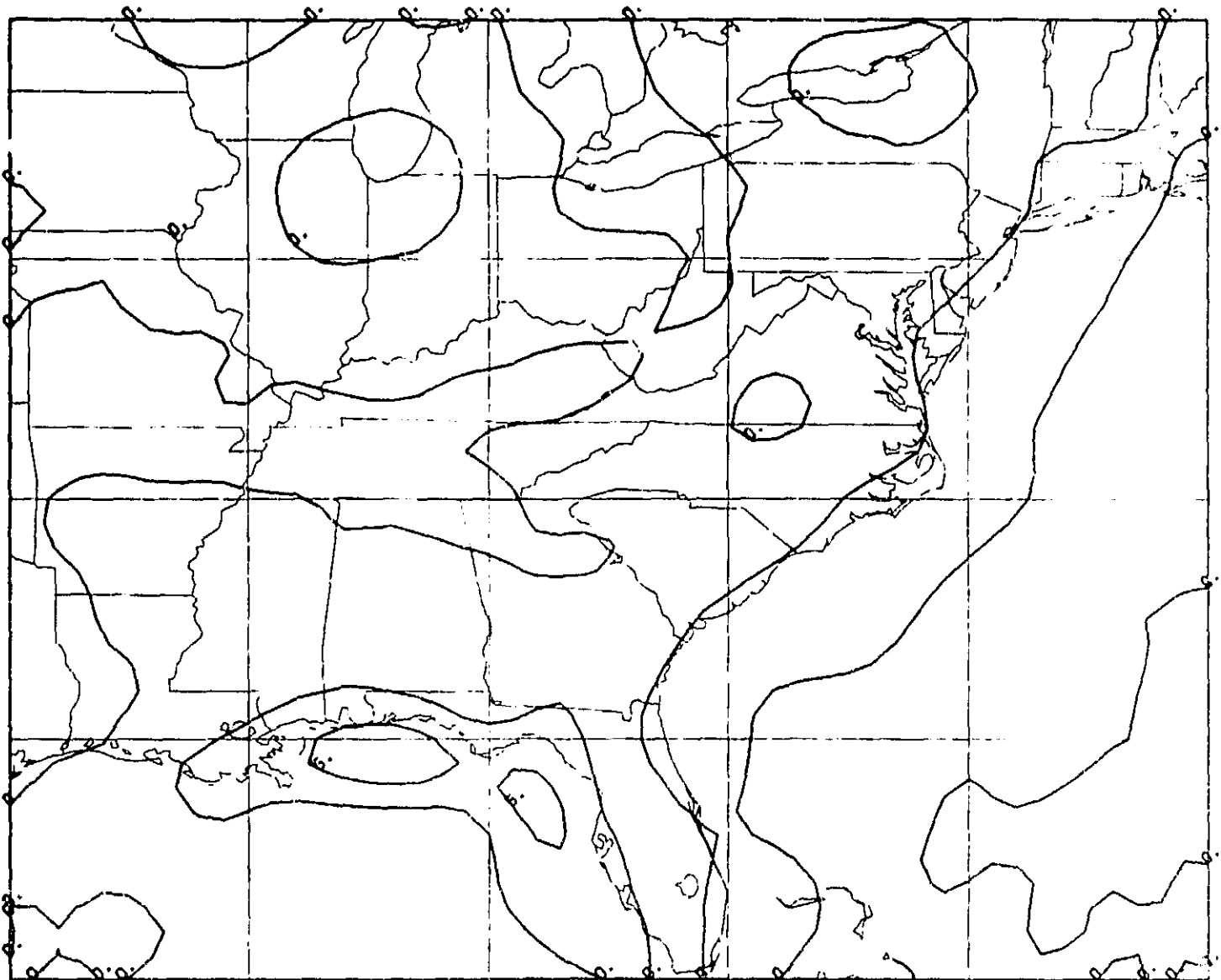


Fig. 17 Difference field ( $T_1 - \tilde{T}$ ) between analyzed temperatures for 12 GMT, 15 January 1979.

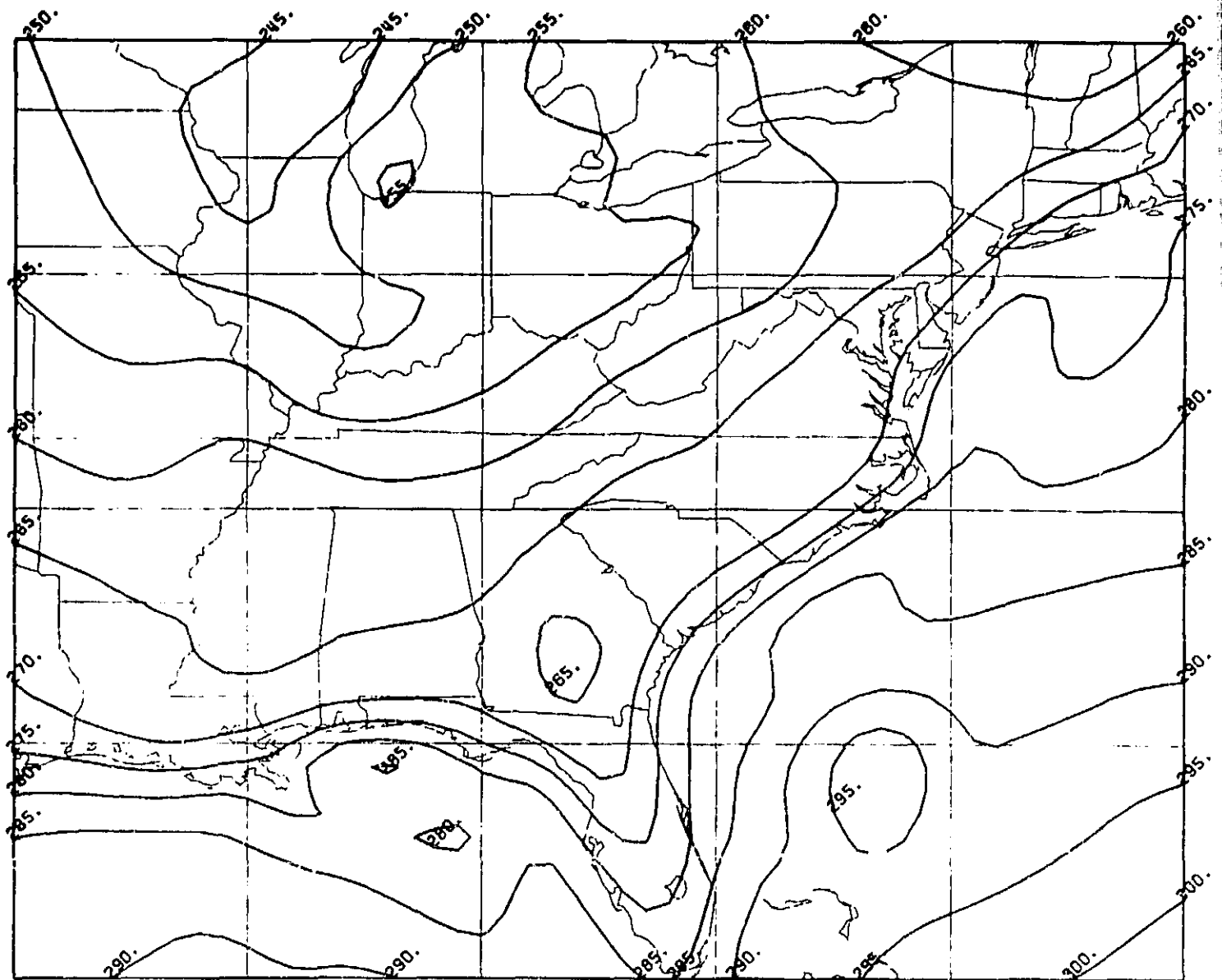


Fig. 18 Variational temperature analysis ( $T_2$ ) for 12 GMT, 15 January 1979  
( $A = 0.1$ ,  $B = C = 3.E9$ ,  $D = E = 3.E18$ ).

ORIGINAL  
OF POOR QUALITY

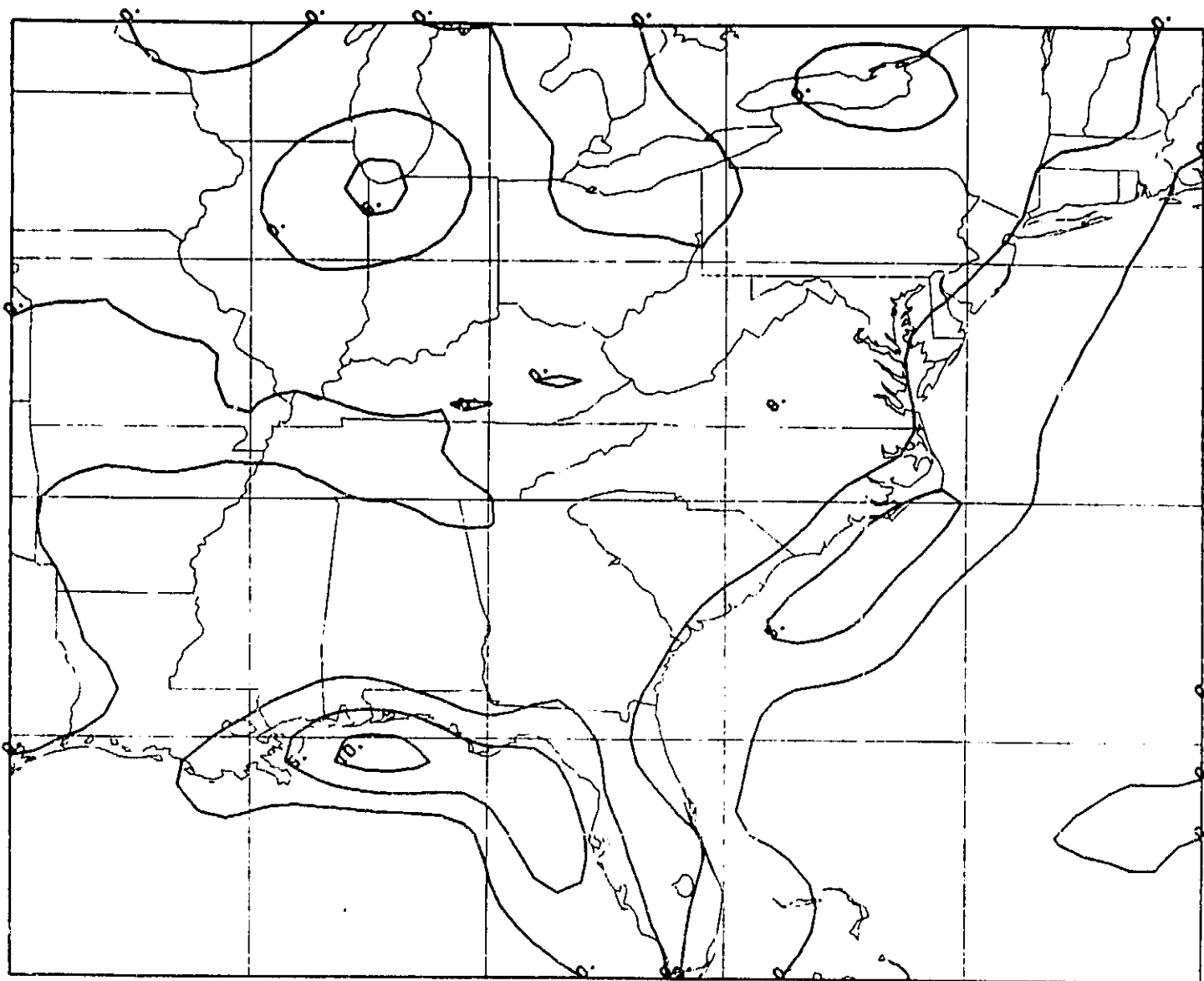


Fig. 19      Difference field  $(T_2 - \tilde{T})$  between analyzed temperatures for 12 GMT,  
15 January 1979.

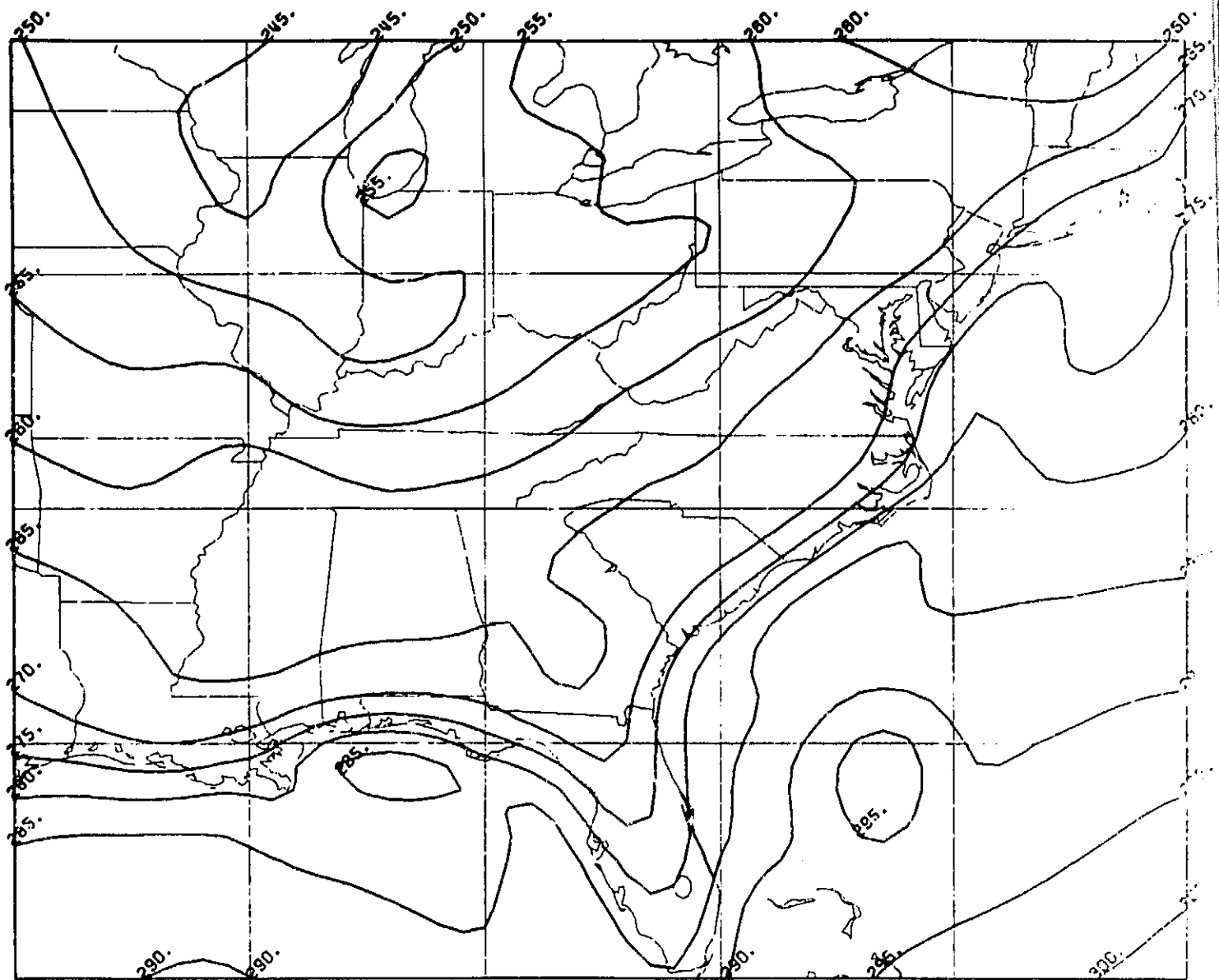


Fig. 20 Variational temperature analysis ( $T_3$ ) for 12 GMT, 15 January 1979  
( $A = 0.1$ ,  $B = C = 1.E10$ ,  $D = E = 1.E19$ ).



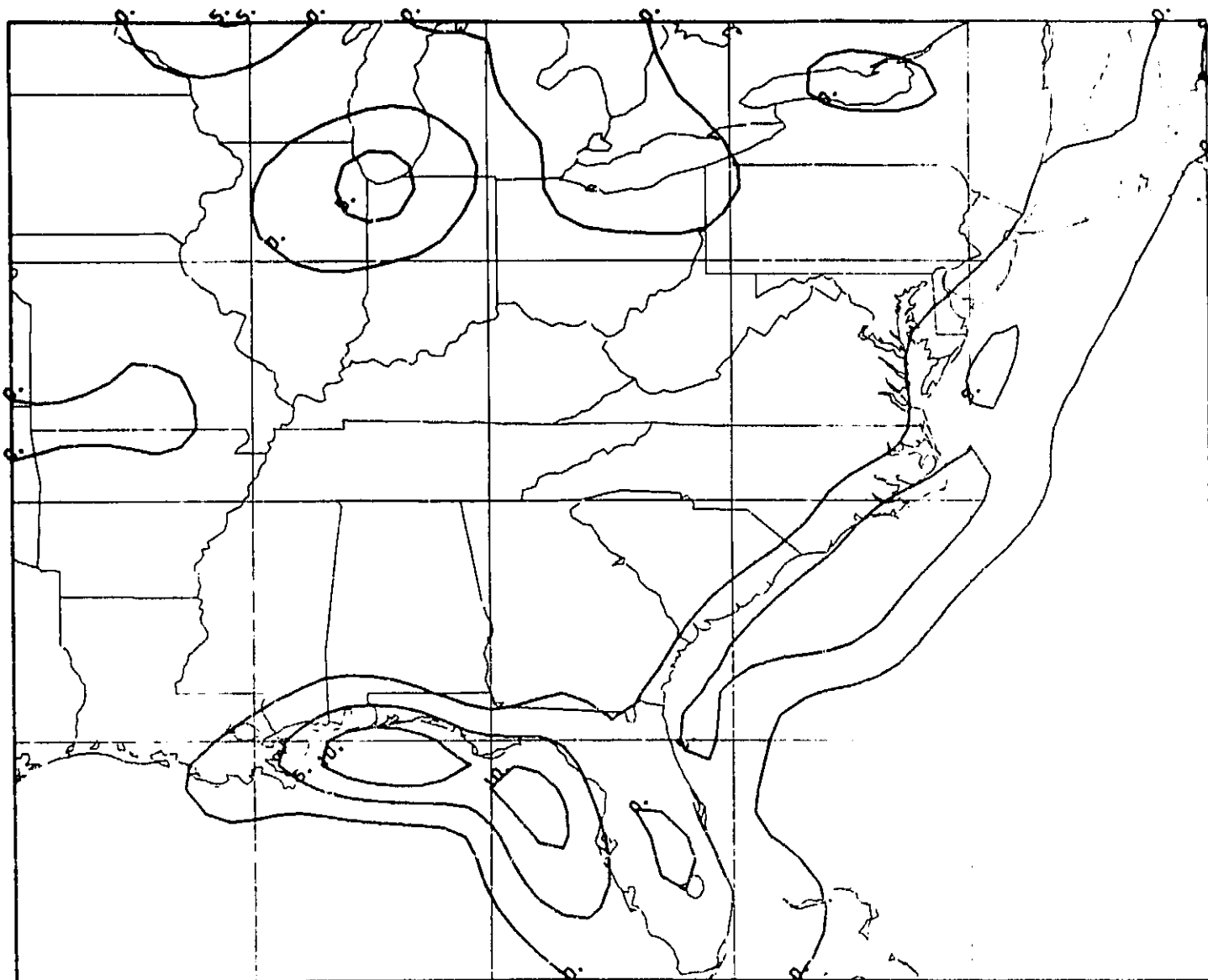


Fig. 21 Difference field ( $T_3 - \tilde{T}$ ) between analyzed temperatures for 12 GMT, 15 January 1979.

temperature information increases, the resulting fields are such that their gradients and Laplacians more closely match those for  $\hat{T}$ -field while at the same time they less closely match the surface observations of temperature. As the difference field in Fig. 15 would suggest, it can be seen in Figs. 17, 19, and 21 that the major impact of the satellite information is upon the coastal areas of the southeastern U.S.

#### 4. MESOSCALE MODEL

The forecast model used in this study is a dry version of the CIMMS Mesoscale Model (CMM). It is a limited-area primitive equation model (with terrain) which evolved from the global model described by Sasaki and Goerss (1982). A unique feature of this model is that it employs variational constraints each time step in order to control the total mass and energy within its domain (Sasaki, 1976; 1977). In this section we will briefly outline the features of the CMM.

The model uses spherical coordinates with  $\sigma$  as the vertical coordinate. It employs a staggered latitude-longitude grid using the Arakawa (C) lattice (Mesinger and Arakawa, 1976) as illustrated in Fig. 22 for  $0.5^\circ$  grid spacing. Values of  $\pi$ ,  $T$ ,  $\delta$ , and  $\phi$  are carried at the grid points labeled A. The vertical structure of the model is also shown in Fig. 22. The number of levels where  $\bar{v}$  and  $T$  are carried is denoted by KM. The value of  $\sigma$  is zero at the top of the model atmosphere ( $p_t$ ) and is one at the surface ( $p_g$ ). The vertical velocity  $\delta$  is zero at both  $\sigma = 0$  and  $\sigma = 1$ . The model consists of KM layers each 1/KM thick.

The primitive equations are written in flux form using  $(\lambda, \theta, \sigma)$  coordinates:

$$\begin{aligned} \frac{\partial \pi}{\partial t} + \frac{1}{a \cos \theta} \left\{ \frac{\partial}{\partial \lambda} (\pi u) + \frac{\partial}{\partial \theta} (\pi v \cos \theta) \right\} + \frac{\partial}{\partial \sigma} (\pi \dot{\sigma}) &= 0 \\ \frac{\partial}{\partial t} (\pi u) + \frac{1}{a \cos \theta} \left\{ \frac{\partial}{\partial \lambda} (\pi u^2) + \frac{\partial}{\partial \theta} (\pi uv \cos \theta) \right\} + \frac{\partial}{\partial \sigma} (\pi u \dot{\sigma}) \\ + \frac{\pi}{a \cos \theta} \left( \frac{\partial \phi}{\partial \lambda} + \sigma \alpha \frac{\partial \pi}{\partial \lambda} \right) - \left( f + \frac{u \tan \theta}{a} \right) \pi v &= \pi F_\lambda \end{aligned}$$

# HORIZONTAL STRUCTURE

$A_{i-1,j-1}$	$u_{i-1,j}$	$A_{i-1,j}$	$u_{i-1,j+1}$	$A_{i-1,j+1}$
$V_{i-1,j-1}$		$V_{i-1,j}$		$V_{i-1,j+1}$
$A_{i,j-1}$	$u_{i,j}$	$A_{i,j}$	$u_{i,j+1}$	$A_{i,j+1}$
$V_{i,j-1}$		$V_{i,j}$		$V_{i,j+1}$
$A_{i+1,j-1}$	$u_{i+1,j}$	$A_{i+1,j}$	$\uparrow$ $1/4^\circ$ $\downarrow$ $u_{i+1,j+1}$ $\leftarrow 1/4^\circ \rightarrow$	$A_{i+1,j+1}$

A - denotes presence of  $\tau$ ,  $q$ , and  $\pi$  ( $\sigma=1$ )

# VERTICAL STRUCTURE

$\dot{\sigma} = 0, \sigma = 0$
$\bar{V}_{KM}, A_{KM}$
$\dot{\sigma}_{KM-1}, \sigma = \frac{1}{KM}$
$\bar{V}_{KM-1}, A_{KM-1}$
$\dot{\sigma}_{KM-2}, \sigma = \frac{2}{KM}$
$\vdots$
$\dot{\sigma}_2, \sigma = \frac{KM-2}{KM}$
$\bar{V}_2, A_2$
$\dot{\sigma}_1, \sigma = \frac{KM-1}{KM}$
$\bar{V}_1, A_1$
$\dot{\sigma} = 0, \sigma = 1$

-33-

Fig. 22 Horizontal and vertical structure of the CIMMS Mesoscale Model.

$$\frac{\partial}{\partial t} (\pi v) + \frac{1}{a \cos \theta} \left\{ \frac{\partial}{\partial \lambda} (\pi u v) + \frac{\partial}{\partial \theta} (\pi v^2 \cos \theta) \right\} + \frac{\partial}{\partial \sigma} (\pi v \dot{\sigma})$$

$$+ \frac{\pi}{a} \left( \frac{\partial \phi}{\partial \theta} + \sigma \alpha \frac{\partial \pi}{\partial \theta} \right) + \left( f + \frac{u \tan \theta}{a} \right) \pi u = \pi F_{\theta}$$

$$\frac{\partial}{\partial t} (\pi T) + \frac{1}{a \cos \theta} \left\{ \frac{\partial}{\partial \lambda} (\pi u T) + \frac{\partial}{\partial \theta} (\pi v T \cos \theta) \right\} + \left( \frac{p}{1000} \right)^{\kappa} \frac{\partial}{\partial \sigma} (\pi \dot{\sigma} \theta)$$

$$+ \frac{\pi^2 \sigma \alpha}{c_p} \left[ \frac{1}{a \cos \theta} \frac{\partial u}{\partial \lambda} + \frac{\partial}{\partial \theta} (v \cos \theta) \right] + \frac{\partial \dot{\sigma}}{\partial \sigma} = \frac{\pi Q}{c_p}$$

where  $\pi = p_g - p_t$  and  $p = \pi \sigma + p_t$ . The value of  $p_t$  is 150 mb. Except for friction in the lowest  $\sigma$ -layer, no parameterization of irreversible physical processes was included in this study. The model integrations are carried out using centered-time and centered-space finite differencing in order to forecast  $\pi$ ,  $u$ ,  $v$ , and  $T$ . After the forecast for  $\pi$  at time  $n+1$  has been made, diagnostic equations are solved for the values of  $\dot{\sigma}$  and  $\phi$  at time  $n$  and the results are used in forecasting  $u$ ,  $v$ , and  $T$  at time  $n+1$ .

The CMM employs only very simple and computationally compact finite differencing while variational adjustments are made each time step in order to control the total mass and energy within the model domain. The values for these quantities are diagnosed either from the larger scale model (if any) the CMM is nested within or from the analyzed fields which provide the CMM with its lateral boundary conditions.

For a given time step, in order to control the mass within the CMM domain we minimize the functional:

$$I = \sum_i \sum_j (\pi - \tilde{\pi})^2 \Delta A + \lambda_M \left( \sum_i \sum_j \pi \Delta A - M \right),$$

where  $M$  is the total mass within the model domain at that time step as determined from the larger scale model or the analyzed fields,  $\Delta A$  is the increment of area associated with each model grid point,  $\tilde{\pi}$  is the current model solution, and  $\pi$  is the adjusted value. The resulting correction to the  $\pi$ -field is:

$$\pi = \tilde{\pi} - \lambda_M/2$$

$$\text{where } \lambda_M = 2(\sum_i \sum_j \tilde{\pi} \Delta A - M) / \sum_i \sum_j \Delta A.$$

This correction is applied at each time step.

To control the total energy within the model domain each time step, the following functional is minimized:

$$J = \sum_i \sum_j \sum_k \{ \alpha [(u - \tilde{u})^2 \Delta A_u + (v - \tilde{v})^2 \Delta A_v] + \beta (T - \tilde{T})^2 \Delta A_T \}$$

$$+ \lambda_E \left[ \sum_i \sum_j \sum_k (c_p \pi_T T \Delta A_T + \pi_u u^2 \Delta A_u / 2 + \pi_v v^2 \Delta A_v / 2) - TE \right],$$

where  $TE$  is the total energy within the model domain at that time step as determined from the larger scale model or the analyzed fields;  $\Delta A$  is the increment of area associated with each model grid point;  $\tilde{u}$ ,  $\tilde{v}$ , and  $\tilde{T}$  are the current model solutions while  $\pi$  is the result of the previous variational adjustment; and  $u$ ,  $v$ , and  $T$  are the adjusted values. The weights  $\alpha$  and  $\beta$  are chosen so that their ratio is  $T/c_p \approx 0.272$ . The resulting corrections for  $u$ ,  $v$ , and  $T$  are:

$$\begin{aligned} u &= \tilde{u}(1 - \lambda_E \pi_u / 2\alpha) , \\ v &= \tilde{v}(1 - \lambda_E \pi_v / 2\alpha) , \\ \text{and } T &= \tilde{T} - \lambda_E c_p \pi_T / 2\beta . \end{aligned}$$

An approximate solution for  $\lambda_E$  is used:

$$\lambda_E = \frac{\sum_i \sum_j \sum_k (c_p \pi_T \tilde{T} \Delta A_T + \pi_u \Delta A_u \tilde{u}^2 / 2 + \pi_v \Delta A_v \tilde{v}^2 / 2) - TE}{\sum_i \sum_j \sum_k (c_p^2 \pi_T^2 \Delta A_T / 2\beta + \pi_u^2 \Delta A_u \tilde{u}^2 / 2\alpha + \pi_v^2 \Delta A_v \tilde{v}^2 / 2\alpha)}$$

Finally, in order to compensate for the adjustment to  $\pi$  and its effect upon the energy calculation,  $\lambda_E$  is adjusted by the ratio  $\sum_i \sum_j \tilde{\pi} \Delta A / M$  before the adjustments for  $u$ ,  $v$ , and  $T$  are computed.

Normally a "double-nesting" procedure is employed with the CMM nested within a coarser resolution version of itself which in turn can either be nested within the global model or have its boundaries specified in some other fashion. For example, a  $1^\circ$  resolution version of the CMM might be used to make a 12-hour forecast beginning at 12 GMT with its boundary tendencies determined from analyzed fields at 12 GMT, 18 GMT, and 00 GMT or from the forecast fields obtained from a  $2^\circ$  resolution version of the global model. Then forecasts could be made using a  $0.5^\circ$  resolution version of the CMM whose domain would be in the center of the  $1^\circ$  version's domain and whose boundary tendencies are determined from the forecast field produced by the  $1^\circ$  model.

The lateral boundary conditions employed in the CMM are those developed by Perkey and Kreitzberg (1976). They allow changes outside the limited domain to influence results there without contaminating the forecast with spurious boundary reflected energy. Their boundary condition transforms long- and medium-length interior advective and gravity waves into short waves that can be removed by a low-pass filter. For any prognostic variable  $X$  and time  $n+1$ ,

$$X_{n+1}(I) = X_{n-1}(I) + W(I) \frac{\partial X_m}{\partial t} \Big|_{I,n} \Delta t + (1 - W(I)) \frac{\partial X_l}{\partial t} \Big|_{I,n} \Delta t$$

where  $l$  specifies the large-scale tendency of  $X$  and  $m$  specifies the model tendency. The weights are given by:

	0.0	$I =$ boundary grid points
	0.4	$I =$ (boundary-1) grid points
$W(I) =$	0.7	$I =$ (boundary-2) grid points
	0.9	$I =$ (boundary-3) grid points
	1.0	$I =$ all other points

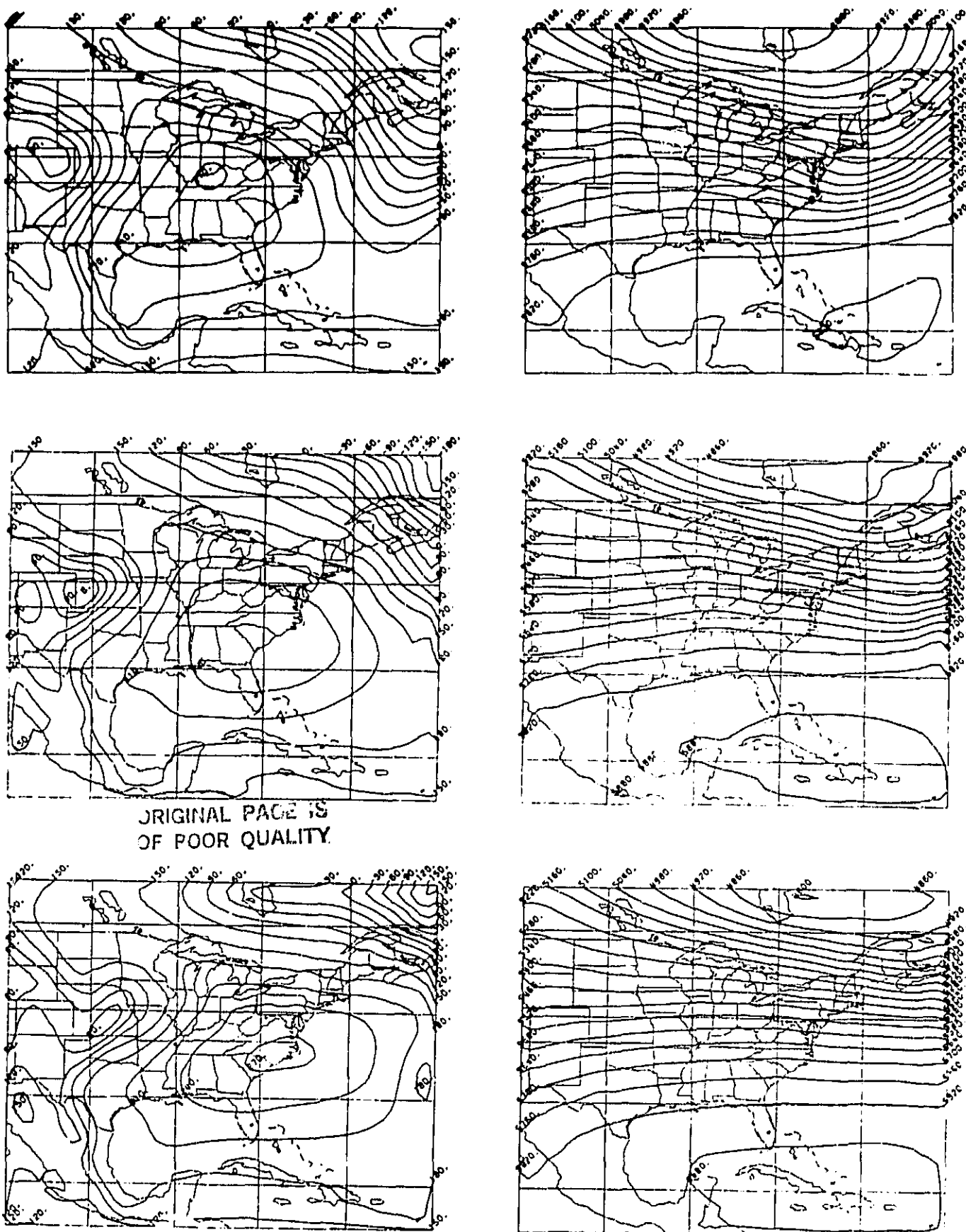
The low-pass filtering is accomplished by using a smoother-desmoother upon the grid points within 7 grid intervals of the boundaries every  $N$ th and  $2N$ th time step and over the entire domain every  $3N$ th time step. The choice of  $N$  is dependent upon the model resolution and the length of its time step. In one-dimension the smoother-desmoother used is:



$$X_1^B = (1 - \alpha)X_1 + \frac{\alpha}{2} (X_{1-1} + X_{1+1})$$

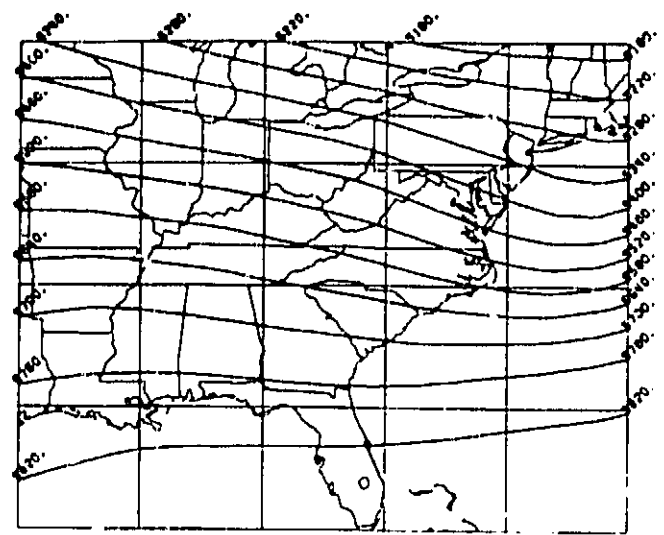
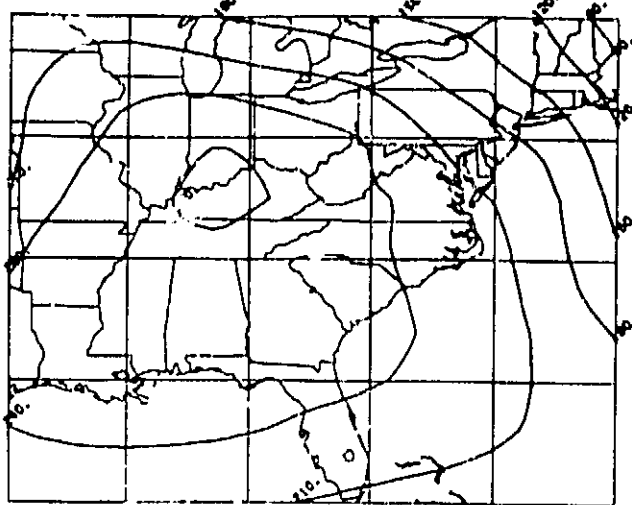
where  $\alpha = 0.50$  on the first pass and  $\alpha = -0.52$  on the second pass.

We now present the results for a 12-hour forecast using the dry version of the CMM with  $0.5^\circ$  grid spacing and twelve  $\sigma$ -layers between the surface ( $p_g$ ) and 150 mb ( $p_t$ ). The  $0.5^\circ$  resolution model was nested within a  $1.0^\circ$  resolution dry version of the CMM with the same vertical structure. The horizontal domains of the models are shown in Figs. 23 and 24. The  $1.0^\circ$  resolution model was initialized at 12 GMT on 15 January 1979 using fields interpolated from the FGGE Level III-b data set valid at that time. The FGGE Level III-b analyses were produced using the European Centre for Medium Range Weather Forecasts (ECMWF) operational system and were available globally at  $1.875^\circ$  resolution and at the 15 standard levels between 1000 mb and 10 mb, inclusive. The boundary tendencies for the  $1.0^\circ$  resolution CMM forecasts were determined by first constructing fields at 18 GMT, 15 January 1979 and at 00 GMT, 16 January 1979 interpolated from the FGGE Level III-b data sets valid at those times. The tendencies were then found by simply interpolating between the 12 GMT and 18 GMT fields and between the 18 GMT and 00 GMT fields. In Fig. 23 we see the initial 1000 mb and 500 mb height fields for the  $1.0^\circ$  resolution model at 12 GMT, 15 January 1979 along with the forecasts valid at 18 GMT, 15 January 1979 and 00 GMT, 16 January 1979, respectively. We can see in this figure that the Perkey-Kreitzberg boundary scheme appears to be quite effective.



ORIGINAL PAGE IS  
OF POOR QUALITY

Fig. 23 Initial (top), 6-hour forecast (middle), and 12-hour forecast (bottom) 1000 mb and 500 mb height fields from 12 GMT, 15 January 1979 run of the 1.0° resolution, dry version of the CIMMS Mesoscale Model.



ORIGINAL PAGE IS  
OF POOR QUALITY

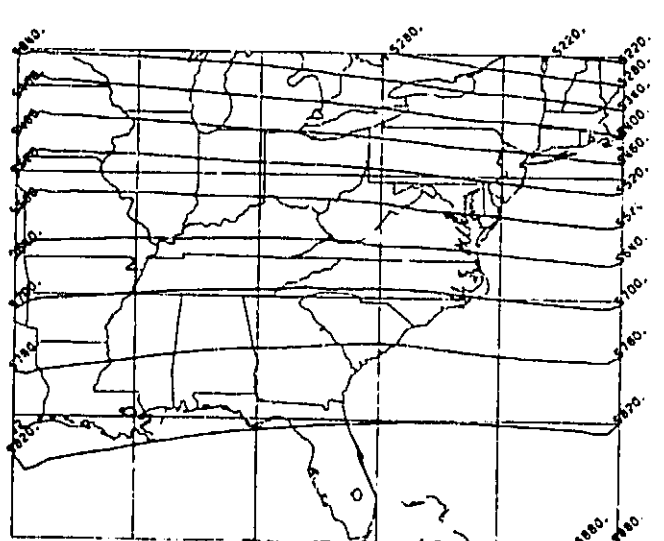
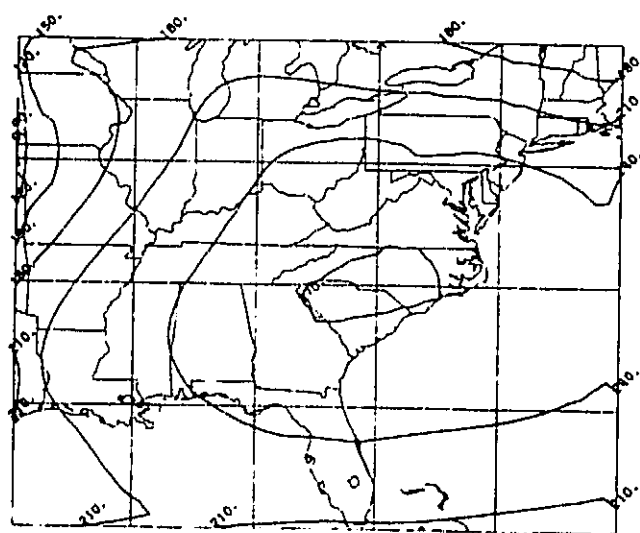
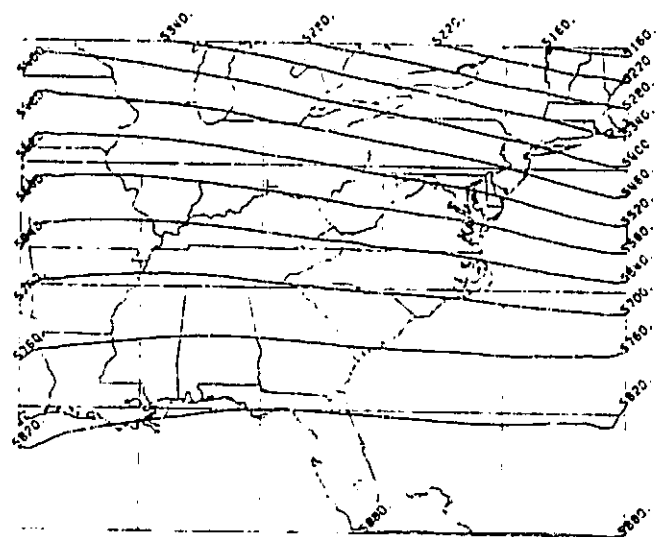
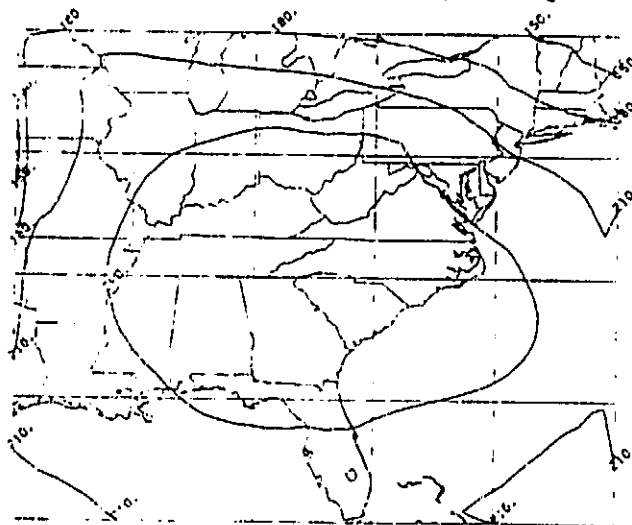
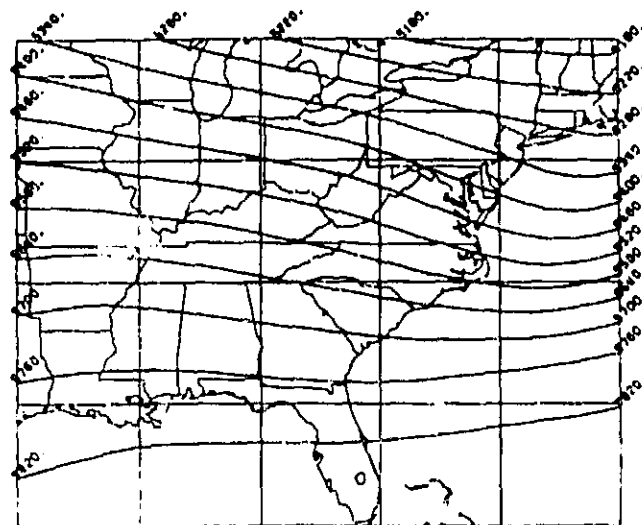
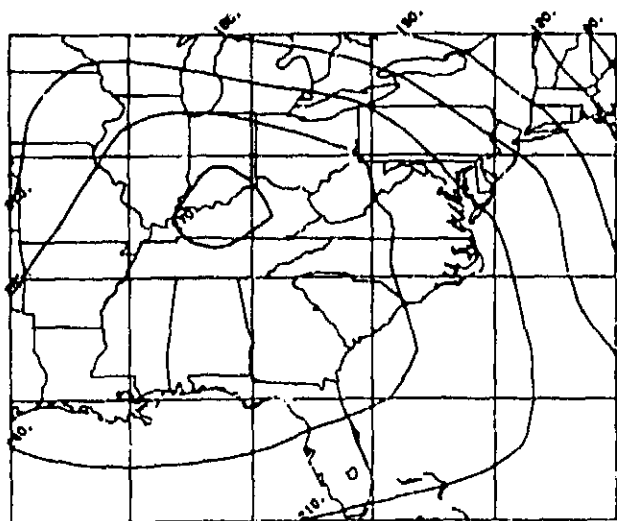
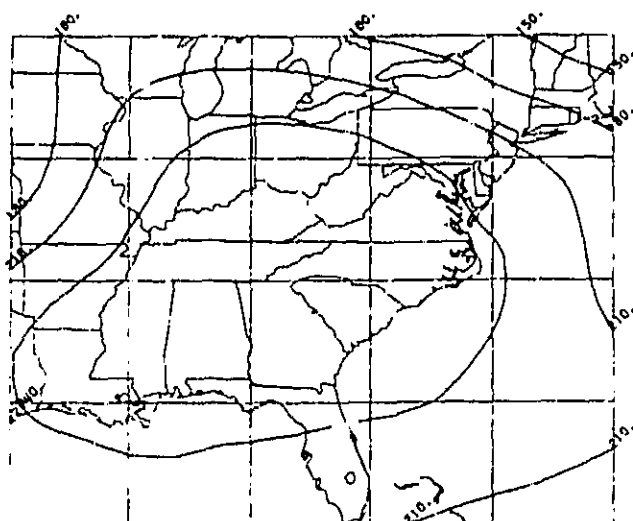


Fig. 24 Initial (top), 6-hour forecast (middle), and 12-hour forecast (bottom) 1000 mb and 500 mb height fields from 12 GMT, 15 January 1979 run of the 0.5° resolution, dry version of the CIMMS Mesoscale Model.



ORIGINAL DATA  
OF POOR QUALITY



The  $0.5^\circ$  resolution model was initialized at 12 GMT, 15 January 1979 with fields interpolated from the  $1.0^\circ$  resolution model. The initial 1000 mb and 500 mb height fields are shown in Fig. 24 along with the forecast fields valid at 18 GMT and 00 GMT, respectively. The boundary conditions for the  $0.5^\circ$  resolution model were obtained by linearly interpolating between forecast fields produced by the  $1.0^\circ$  resolution model at 2-hour intervals between 12 GMT and 00 GMT. Again we see that the Perkey-Kreitzberg boundary scheme works well.

Finally, in Fig. 25 verification fields interpolated from the FGGE Level III-b data sets valid at 12 GMT and 18 GMT, 15 January 1979 and at 00 GMT, 16 January 1979 are displayed. Comparing Figs. 24 and 25 we can see that the CMM forecasts of 1000 mb and 500 mb heights are quite reasonable.

## 5. ASSIMILATION EXPERIMENT

Ultimately, one would like to use satellite temperature data to improve the forecasts made by mesoscale models. In the previous sections we have examined the conventional and satellite data available, a variational temperature analysis scheme designed to combine these data, and the CMM which will be used to test the impact of data assimilation. Since the TIROS-N data is such that one can normally expect virtually all of a mesoscale model domain to be covered by one pass of the satellite, the data assimilation problem is really an initialization problem. Whenever a satellite pass occurs the entire model domain would be re-initialized at that time. Thus, we have an intermittent assimilation problem rather than the continuous assimilation problem that one normally encounters when dealing with satellite temperature data assimilation into a global model where a small portion of the model domain is modified each time-step as new satellite data become available. In this section we shall describe three different initialization procedures for the CMM and test their effectiveness at assimilating the satellite temperature information into the CMM. Using the data from 15 January 1979 the impact of satellite temperature assimilation will be evaluated by comparing CMM forecasts made with and without satellite data for all three different initialization schemes.

### Initialization Procedures

Each of the model initialization procedures used in this study consists of some form of objective analysis performed upon the standard pressure surfaces at the horizontal grid-points used by the model. The fields used to

initialize the model are then produced by vertical interpolation from these objectively analyzed fields to the model's  $\sigma$ -coordinate system.

The first initialization procedure we shall consider is the three-dimensional multivariate variational objective analysis procedure described by Sasaki and Goerss (1982). Objectively analyzed fields of geopotential height and winds are produced by minimizing the functional

$$\begin{aligned}
 J = & \iiint [A(\phi - \hat{\phi})^2 + B(\frac{1}{R} \frac{\partial \phi}{\partial \pi} - \hat{T})^2 + C_u(u - \hat{u})^2 + C_v(v - \hat{v})^2 \\
 & + d(\nabla \phi - \nabla \hat{\phi})^2 + e(\nabla^2 \phi - \nabla^2 \hat{\phi})^2 + f(\xi - \hat{\xi})^2 + g(D - \hat{D})^2 \\
 & + h(\frac{1}{a \cos \theta} \frac{\partial \phi}{\partial \lambda} - f_v)^2 + i(\frac{1}{a} \frac{\partial \phi}{\partial \theta} + f_u)^2] d\lambda d\theta d\pi,
 \end{aligned}$$

where

$$\nabla \phi = \frac{1}{a \cos \theta} \frac{\partial \phi}{\partial \lambda} + \frac{1}{a} \frac{\partial \phi}{\partial \theta}$$

$$\nabla^2 \phi = \frac{1}{a^2 \cos^2 \theta} \frac{\partial^2 \phi}{\partial \lambda^2} + \frac{1}{a^2 \cos \theta} \frac{\partial}{\partial \theta} (\cos \theta \frac{\partial \phi}{\partial \theta})$$

$$\xi = \frac{1}{a \cos \theta} \left( \frac{\partial v}{\partial \lambda} - \frac{\partial (u \cos \theta)}{\partial \theta} \right)$$

$$D = \frac{1}{a \cos \theta} \left( \frac{\partial u}{\partial \lambda} + \frac{\partial (v \cos \theta)}{\partial \theta} \right) \quad \text{and}$$

$$\pi = \ln \left( \frac{1000}{p} \right).$$

The resulting values of geopotential height, u-wind, and v-wind are denoted by  $\phi$ ,  $u$ , and  $v$ , respectively, while their corresponding first-guess field values are denoted by  $\tilde{\phi}$ ,  $\tilde{u}$ , and  $\tilde{v}$ . Three-dimensional data weight matrices  $A$ ,  $B$ ,  $C_u$ , and  $C_v$  contain relatively high values at locations of observed geopotential height, temperature, u-wind, and v-wind ( $\hat{\phi}$ ,  $\hat{T}$ ,  $\hat{u}$ , and  $\hat{v}$ ) and negligible values elsewhere. The weights  $d$ ,  $e$ ,  $f$ ,  $g$ ,  $h$ , and  $i$  are constant over most of the domain but are set to zero near the boundaries in order to satisfy certain boundary conditions. Each weight is assigned a value equal to the inverse of the expected variance of the difference it is associated with in the functional  $J$ .

The solution of this variational problem over the domain results in fields of geopotential height, u-wind, and v-wind:

- 1) which agree with the surface and upper-air observations;
- 2) for which the horizontal gradients and Laplacians of geopotential height and the vorticity and divergence of the wind field match those for the first-guess fields;
- 3) for which the vertical derivatives of the geopotential height field are consistent with the observed temperatures; and
- 4) which are in approximate geostrophic balance.

In this study the first-guess fields were interpolated from the FGGE Level III-b data set valid at 12 GMT, 15 January 1979. Surface and upper-air observations from that time were taken from the appropriate FGGE Level II-b data set. Satellite data assimilation was accomplished by replacing the first-guess geopotential height field ( $\tilde{\phi}$ ) with one derived using the temperature fields produced from the variational temperature analysis scheme described in Section 3 and by increasing the relative weighting upon the terms in functional  $J$  containing gradients and Laplacians of  $\tilde{\phi}$ .



The second initialization procedure can be described as a simple two-dimensional univariate objective analysis scheme patterned after that described by Cressman (1959). For each variable (surface pressure, temperature, u-wind, and v-wind) a Cressman analysis is performed using radii of influence based upon the average distance between observations. Surface analyses are produced for pressure and temperature using smaller radii of influence than the analyses of temperature, u-wind, and v-wind performed upon the standard pressure surfaces using the upper air observations. These analyses are performed one variable at a time and one level at a time with no coupling between the variables or the levels. The model is then initialized by interpolating these fields to the model's  $\sigma$ -coordinate system.

The third initialization procedure we shall investigate is identical to the second except that after the individual fields have been analyzed a static balancing procedure is employed. At each level the following variational functional is minimized:

$$I = \int_{\theta_1}^{\theta_2} \int_{\lambda_1}^{\lambda_2} [A(\phi - \tilde{\phi})^2 + B(u - \tilde{u})^2 + C(v - \tilde{v})^2 + d(\frac{1}{a \cos \theta} \frac{\partial \phi}{\partial \lambda} - fv)^2 + e(\frac{1}{a} \frac{\partial \phi}{\partial \theta} + fu)^2] d\lambda d\theta.$$

The values of geopotential height, u-wind, and v-wind derived from the univariate Cressman analyses are denoted by  $\tilde{\phi}$ ,  $\tilde{u}$ , and  $\tilde{v}$ . The resulting values ( $\phi$ ,  $u$ , and  $v$ ) are such that approximate geostrophic balance is achieved at each level. Thus, at each level the mass and momentum variables are coupled. As we shall see later, this coupling provides the forecast model with fields

that are in better balance so that the model integrations are initiated with less gravity wave noise.

### Model Forecasts

A total of six forecast experiments beginning at 12 GMT, 15 January 1979, were conducted for all combinations of the three different initialization procedures with and without satellite temperature data assimilation. The experiments are denoted by two letters with the first letter standing for the initialization procedure (V-three-dimensional, multivariate variational; C-univariate Cressman; C-univariate Cressman with static balancing) and the second letter indicating whether satellite data assimilation has been performed (S-satellite data assimilation; N-no assimilation). Before discussing the results of the forecast experiments we shall first take a look at the effectiveness of the three initialization procedures in terms of providing the model with balanced fields.

An effective measure of the gravity wave noise within a numerical forecast model is the root mean square pressure tendency determined over the model domain time step. As described by Miyakoda et al. (1978) a major problem of data assimilation and of model initialization is the balance between the model's mass and momentum fields. When a model is initialized such that these fields are not in geostrophic balance, a discontinuity is created with the current model solution. The dynamical characteristics of the model fluid enable it to remove this discontinuity in such a way as to maintain a state of approximate geostrophic balance. This geostrophic adjustment process results in the generation and dispersal of inertial gravity waves. Ideally one would

like to initialize a numerical model with mass and momentum fields which not only match the observed values of temperature, pressure and wind but also are balanced to the extent that the model can begin integration with a minimal amount of noise. In Fig. 26 are plotted the root mean square pressure tendencies for the three assimilation forecasts (VS, CS, and GS) from zero to twelve hours of forecast time. We can see that when the forecast model is initialized using the univariate Cressman procedure the level of gravity wave noise starts considerably higher than for the other two procedures. After about 4-5 hours of model integration the noise level has reached that of the other methods. While the variational method has an initial noise level higher than the Cressman procedure with static balancing, it quickly reaches comparable levels and after about four hours of integration reaches a level slightly less than the two Cressman techniques. Thus, as we would expect, the methods which provide for the coupling of the initial mass and momentum fields produce forecasts with reduced levels of gravity wave noise and perhaps the lowest noise levels are realized by the three-dimensional variational initialization procedure which also provides coupling between the vertical levels of the model atmosphere.

Now we shall begin discussion of the forecast experiments themselves. In every case the CMM was initialized at 12 GMT, 15 January 1979, using the surface and upper air observations available from the FGGE Level II-b data set and using as first-guess fields interpolated fields from the FGGE Level III-b data set. For all initialization procedures objectively analyzed fields were produced at the following pressure levels 1000, 925, 850, 775, 700, 600, 500, 400, 350, 300, 250, 225, 200, 175, and 150. The horizontal grid points used

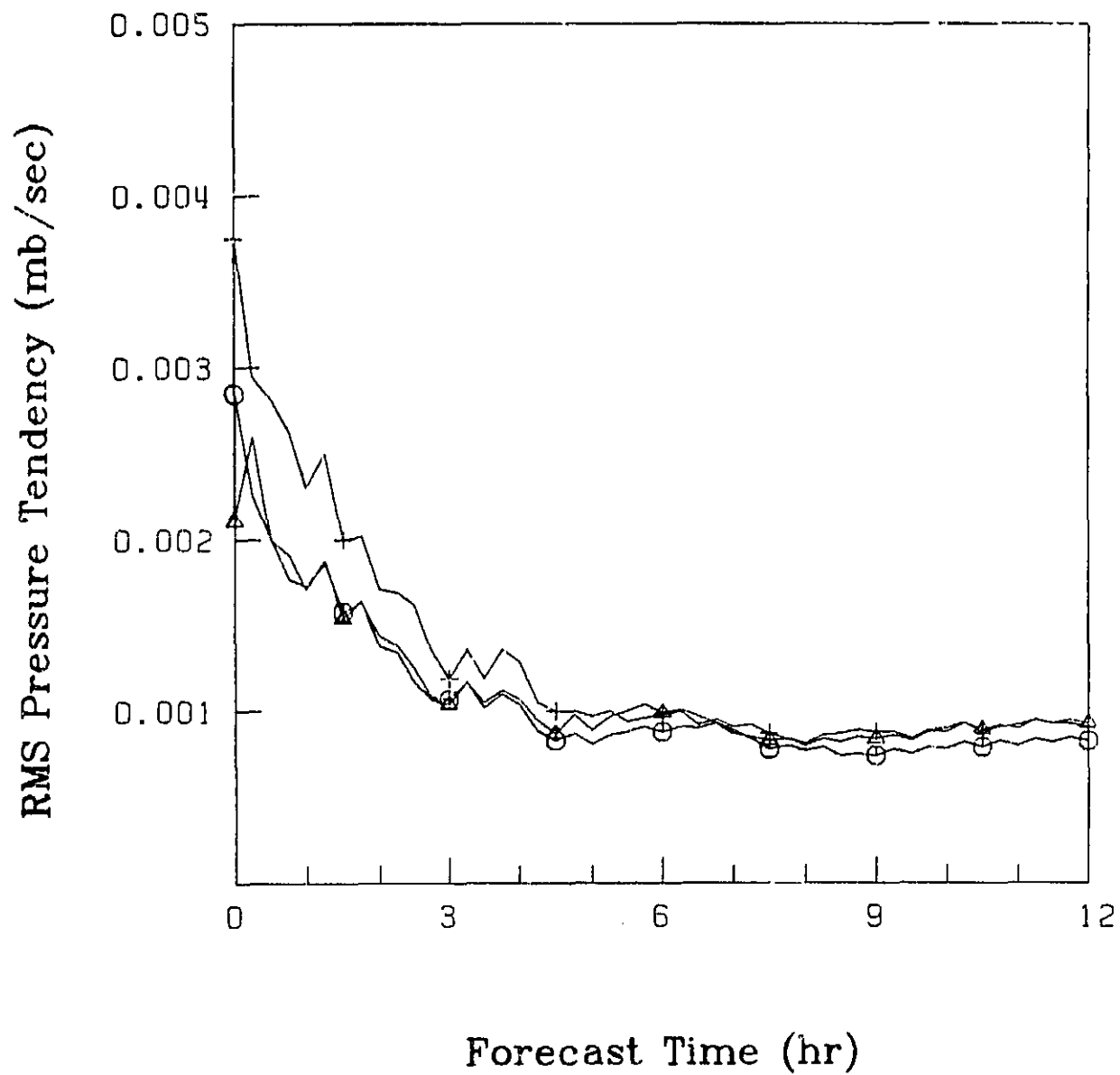


Fig. 26 Root mean square pressure tendencies for VS (circles), CS (crosses), and GS (triangles) 12-hour forecasts from 12 GMT, 15 January 1979.

by each scheme were the same as is used by the CMM. For the assimilation cases the following was done. At the two lowest pressure levels (1000 mb and 925 mb) the Cressman temperature analyses for experiments CS and GS were replaced by the temperature analyses produced by the variational temperature analysis procedure. As discussed previously for the variational case (experiments VS and VN) the first-guess geopotential height field ( $\tilde{\phi}$ ) was replaced by one derived using the temperature fields at 1000 mb and 925 mb produced by the variational temperature analysis scheme. For the non-assimilation experiments (VN, CN and GN) all initial fields were produced by utilizing the respective initialization procedures with conventional observations alone.

We shall now examine the initial fields produced by the different procedures. Since assimilation is only performed in the two lowest levels (1000 mb and 925 mb), the only real differences result there. In Figs. 27-32 are plotted the 1000 mb height and temperature fields for experiments VS, VN, GS, GN, CS, and CN, respectively. In each case we can see the differences between the initial temperature fields for the assimilation and non-assimilation experiments. The variational temperature analysis scheme, as we saw in Section 3, produces low level temperature fields with enhanced gradients in the coastal areas of the southeastern U.S. Comparing the Cressman techniques with the variational one we see that both Cressman techniques produce a deeper closed low in the 1000 mb height field off the Florida Coast while the variational techniques produce a weaker inverted trough. In each case compare the differences between the initialized fields and the first-guess fields interpolated from the FGGE Level III-b data set shown in Fig. 33. As we can see the first-guess fields contain very little detail for either the 1000 mb height or temperature fields.

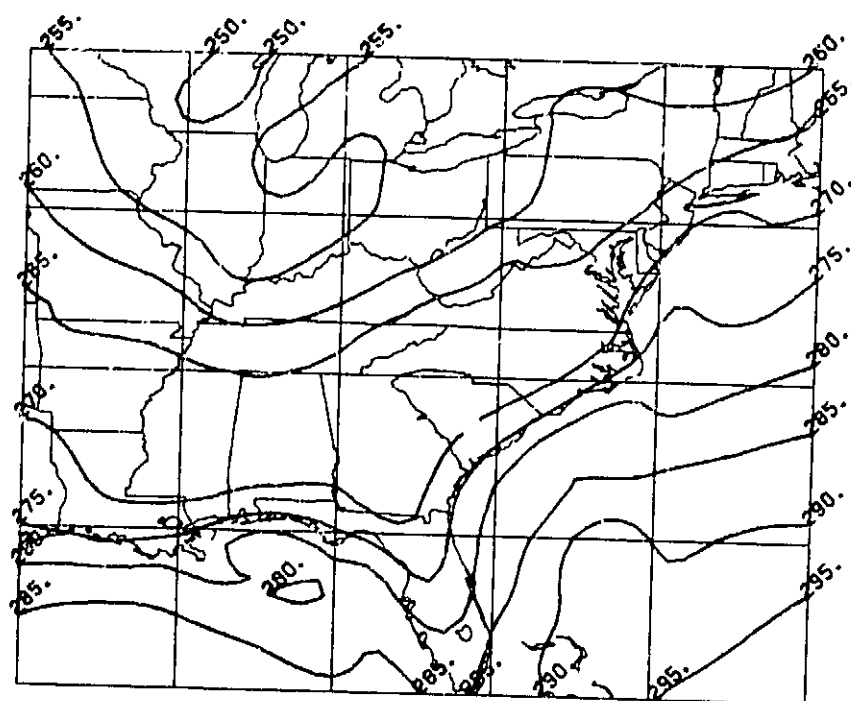


Fig. 27 Initial 1000 mb height (top) and temperature (bottom) fields for experiment VS valid at 12 GMT, 15 January 1979.

ORIGINAL P.  
OF POOR QUALITY

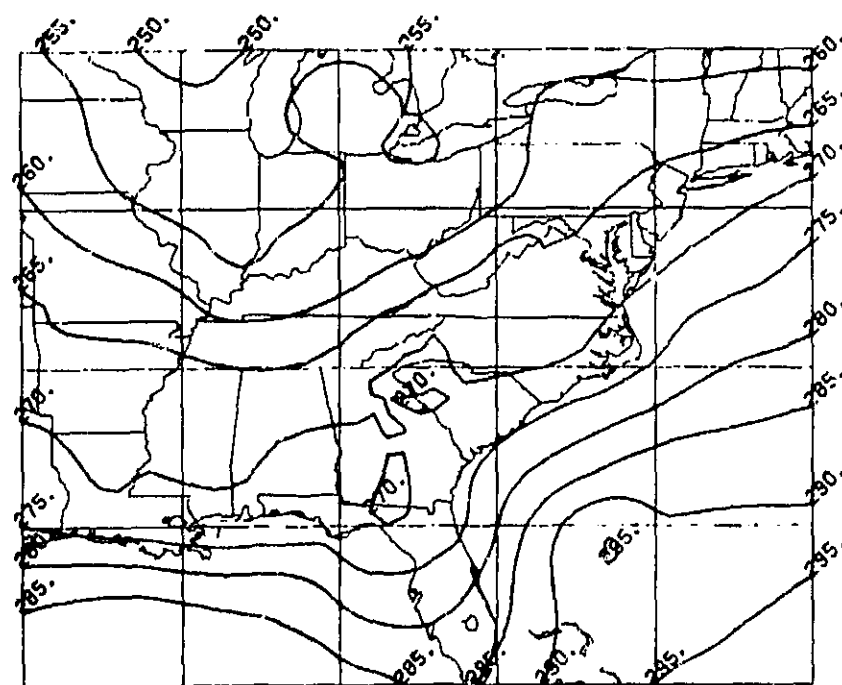
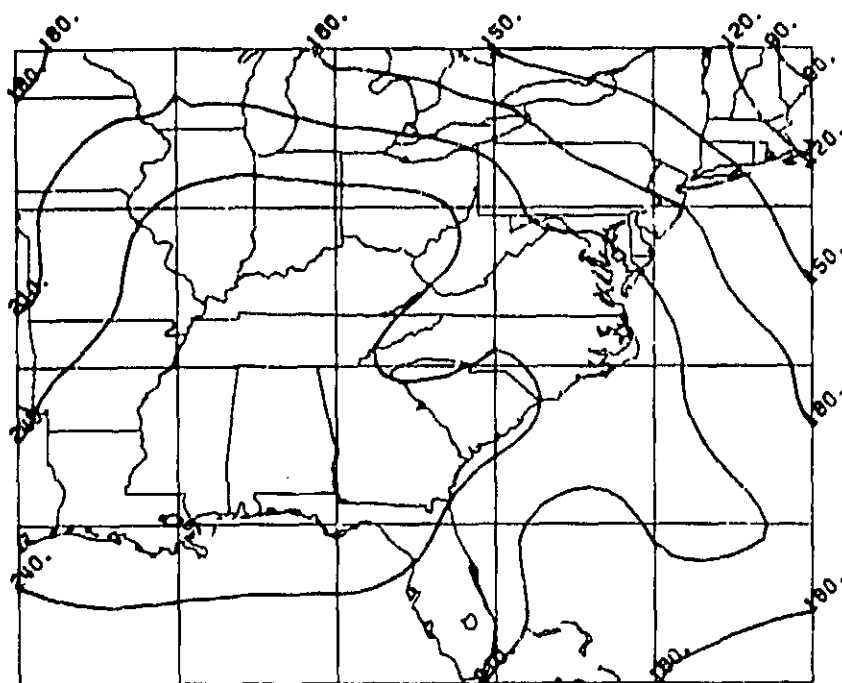


Fig. 28 Initial 1000 mb height (top) and temperature (bottom) fields for experiment VN valid at 12 GMT, 15 January 1979.

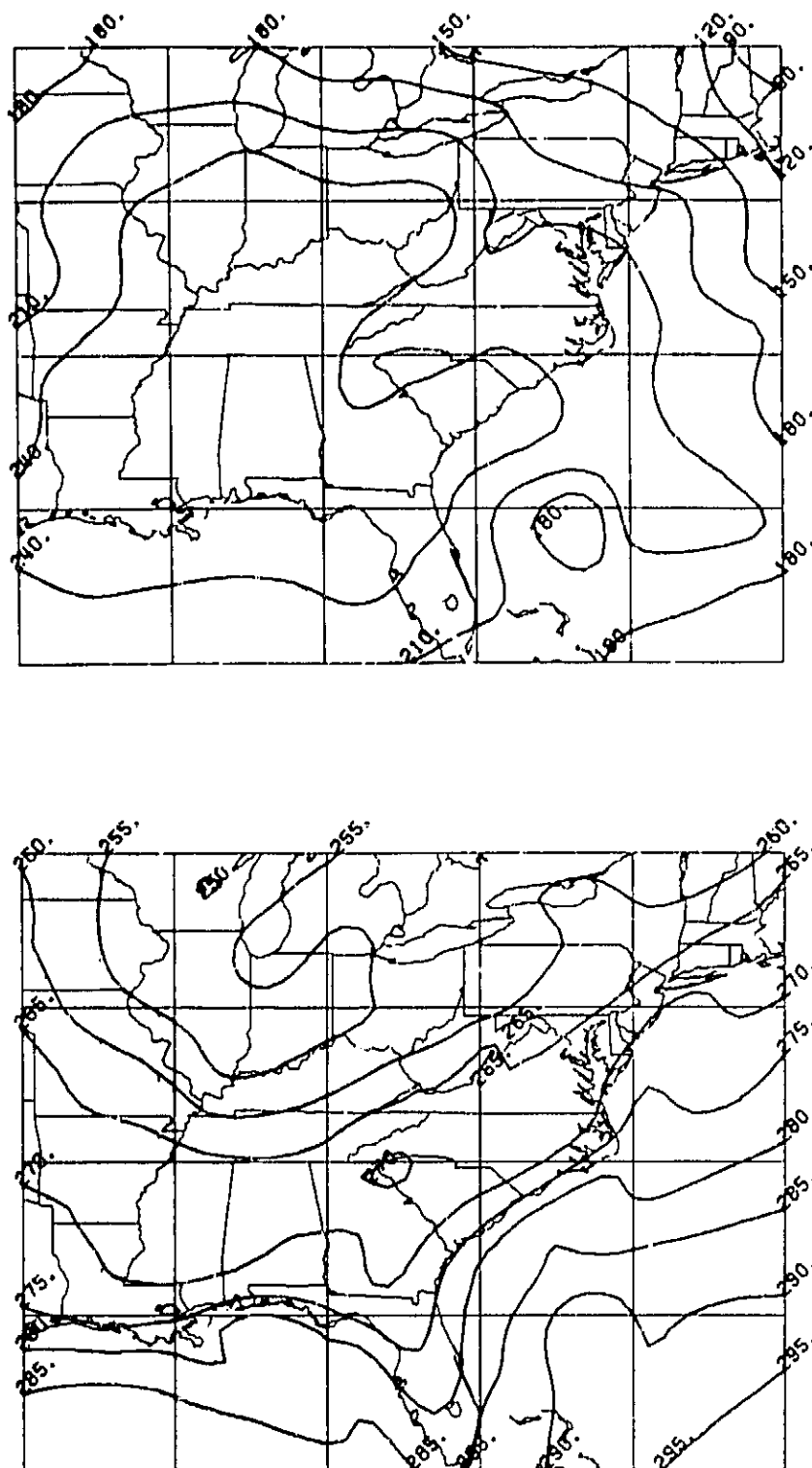


Fig. 29 Initial 1000 mb height (top) and temperature (bottom) fields for experiment GS valid at 12 GMT, 15 January 1979.



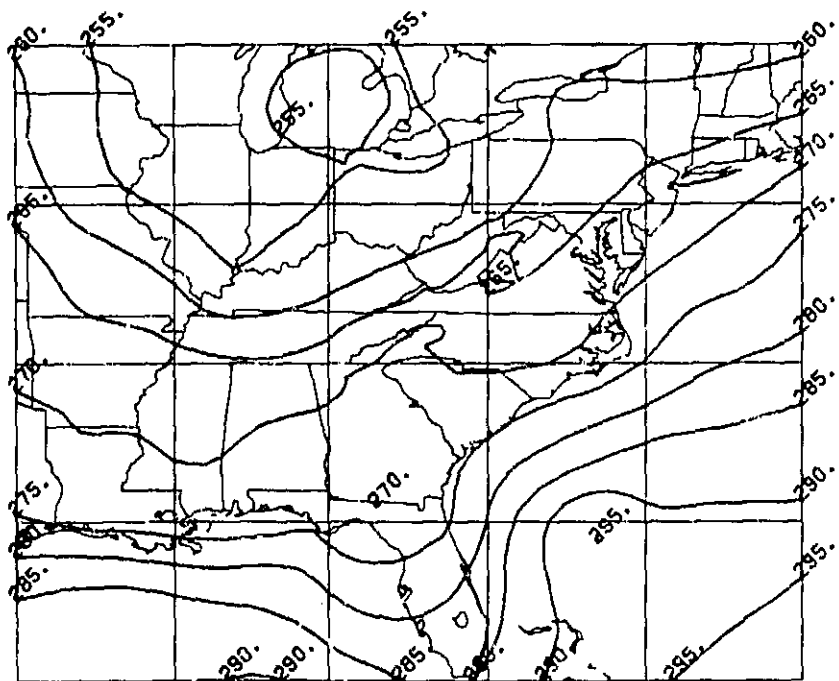
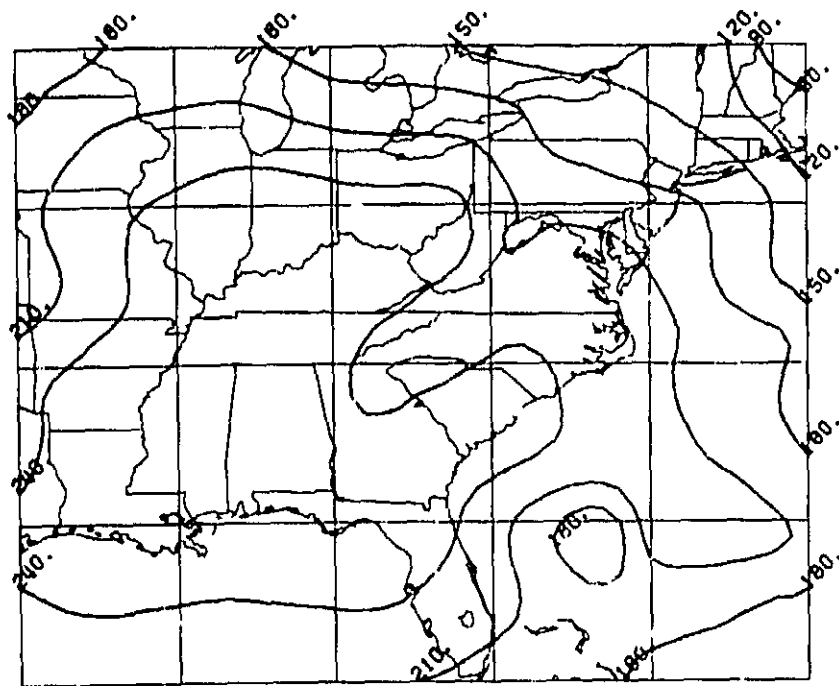


Fig. 30 Initial 1000 mb height (top) and temperature (bottom) fields for experiment GN valid at 12 GMT, 15 January 1979.

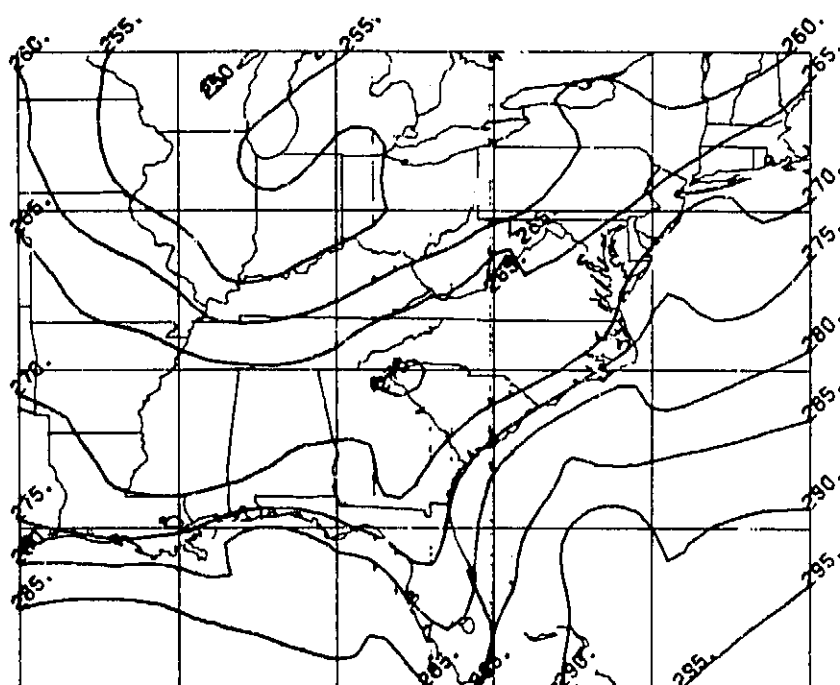
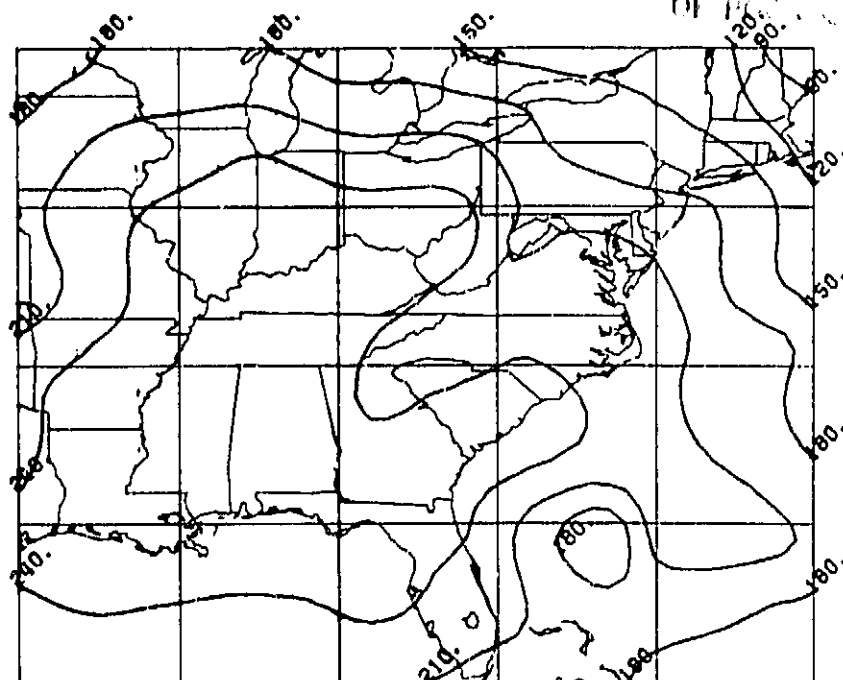


Fig. 31 Initial 1000 mb height (top) and temperature (bottom) fields for experiment CS valid at 12 GMT, 15 January 1979.

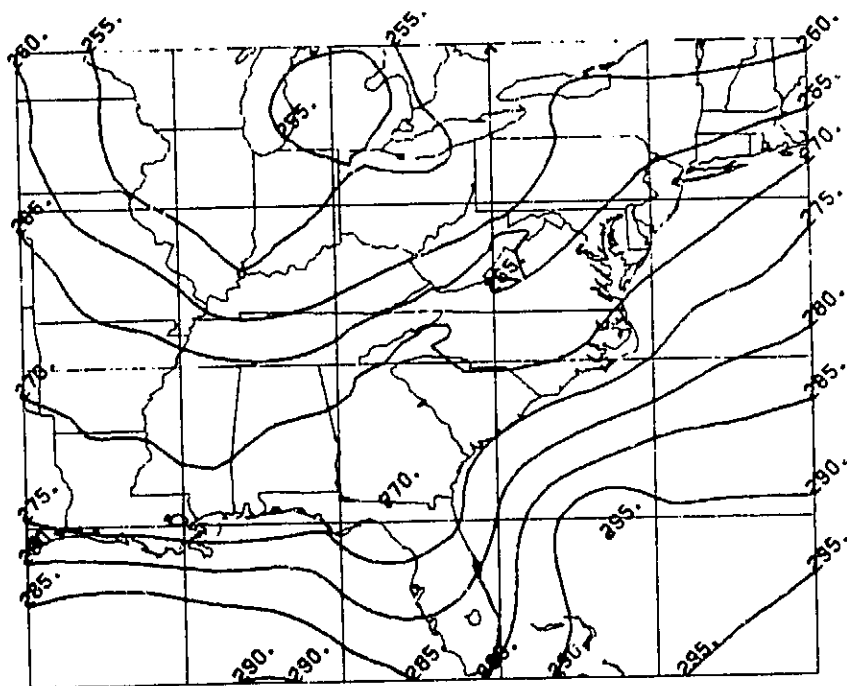
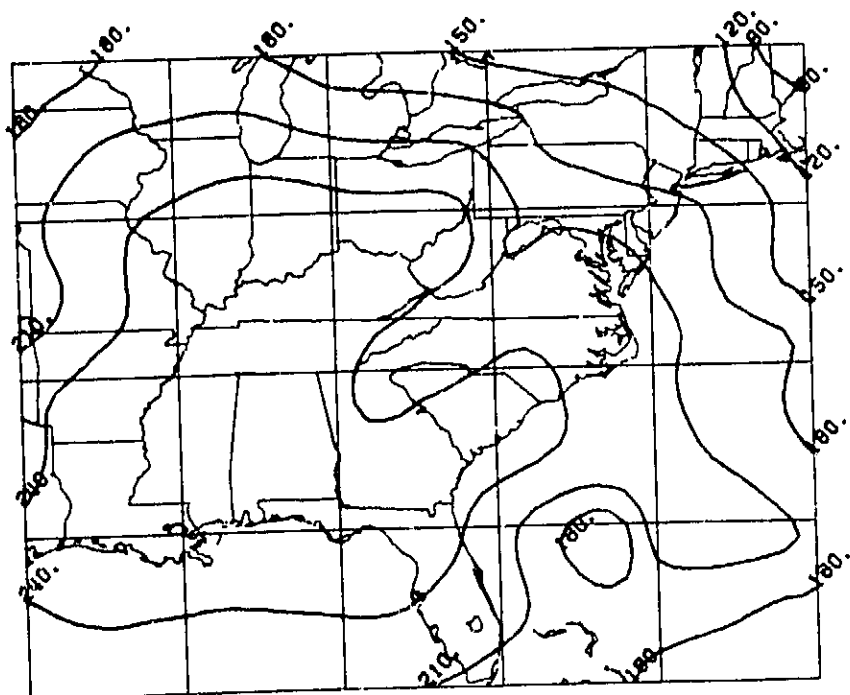


Fig. 32 Initial 1000 mb height (top) and temperature (bottom) fields for experiment CN valid at 12 GMT, 15 January 1979.

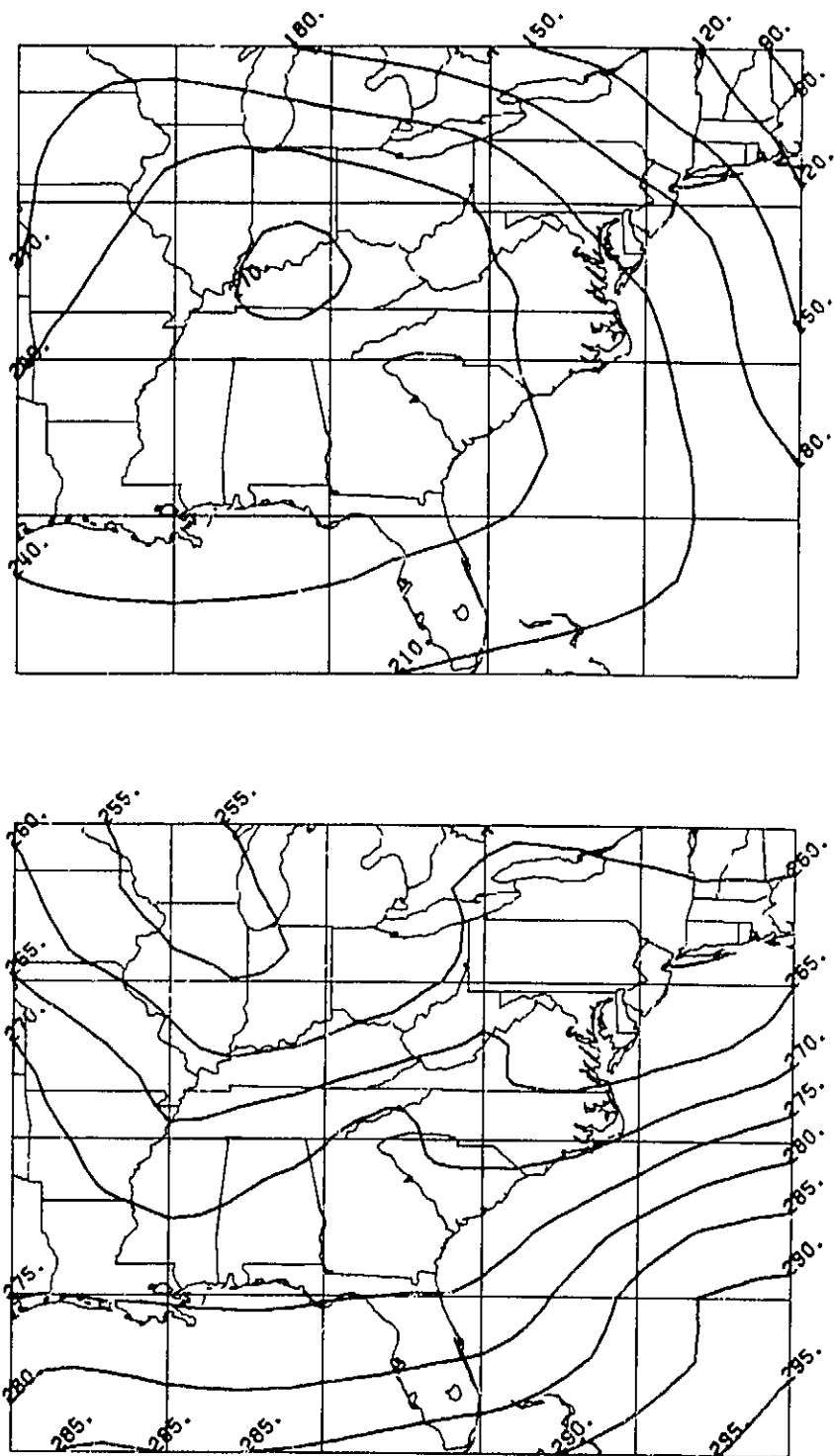


Fig. 33 First-guess 1000 mb height (top) and temperature (bottom) fields interpolated from the FGGE Level III-b data set valid at 12 GMT, 15 January 1979.

The forecast experiments were all conducted using the  $0.5^\circ$  resolution version of the CMM described in Section 4. Forecasts were run out to 24 hours beginning at 12 GMT, 15 January 1979. Boundary tendencies for the  $0.5^\circ$  model were provided every two hours by the  $1.0^\circ$  resolution version of the CMM as discussed in Section 4. The resulting 12-hour forecasts for 1000 mb height and temperature for experiments VS, VN, GS, GN, CS, and CN are shown in Figs. 34-39. The only real difference that is discernible from examination of these figures is the slightly stronger temperature gradient off the southeast coast for the assimilation cases. Subjective comparison of these fields is quite difficult.

In order to objectively compare the 12- and 24-hour forecast fields produced in these experiments we shall compute root mean square errors for the differences between upper-air observations of height at 850 mb and 500 mb and the heights of the forecast fields interpolated to the locations of the observations. We shall also use the FGGE Level III-b fields valid at the forecast times to compute S1 scores (Teweles and Wobus, 1954) for the 850 mb and 500 mb heights. Since there are only about thirty upper air observations available over our domain spaced more widely than the surface observations shown in Fig. 3, the root mean square errors we obtain are hardly conclusive. Similarly, we saw in Fig. 33 how smooth the FGGE Level III-b verifications fields can be. This is a limitation on the use of the S1 scores. However, these data provide the only truly objective means to compare the forecasts. Table 2 summarizes the results of the statistical computations. At 850 mb for the 12-hour forecasts we can see that the only noticeable result is that both VS and VN possess higher skill levels (lower S1 scores) than the Cressman techniques.

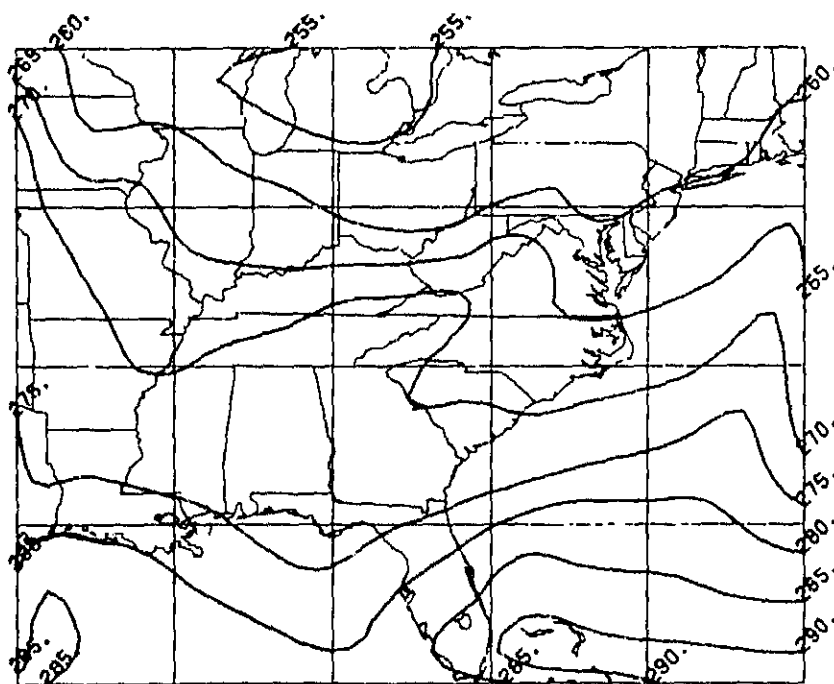
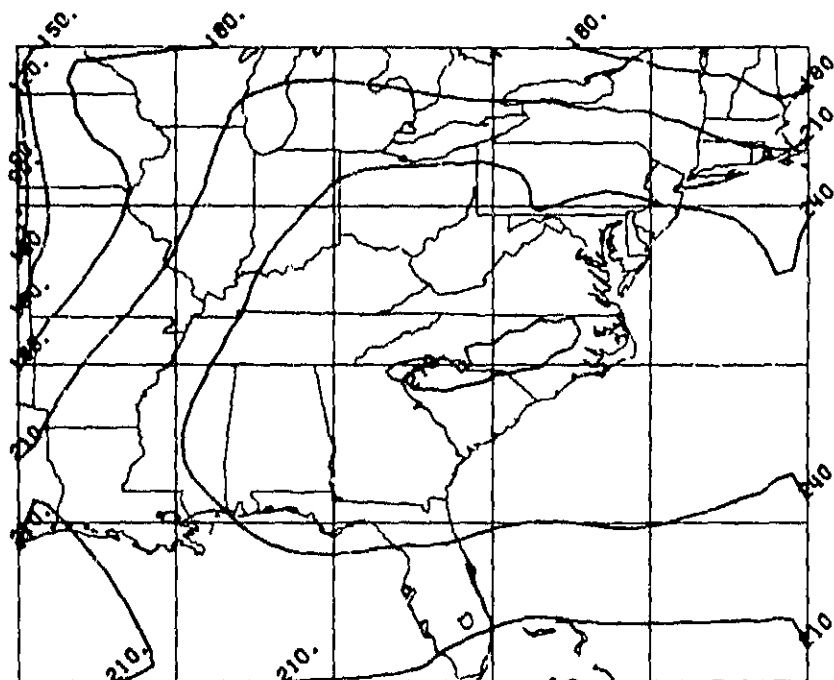


Fig. 34 Twelve-hour forecast 1000 mb height (top) and temperature (bottom) fields for experiment VS valid at 00 GMT, 16 January 1979.

On 16 Jan 79

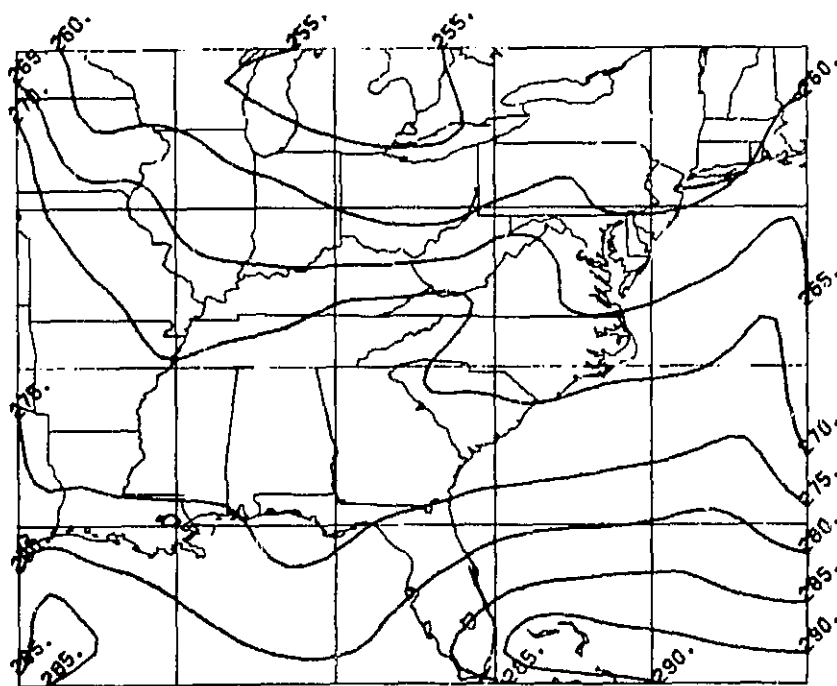
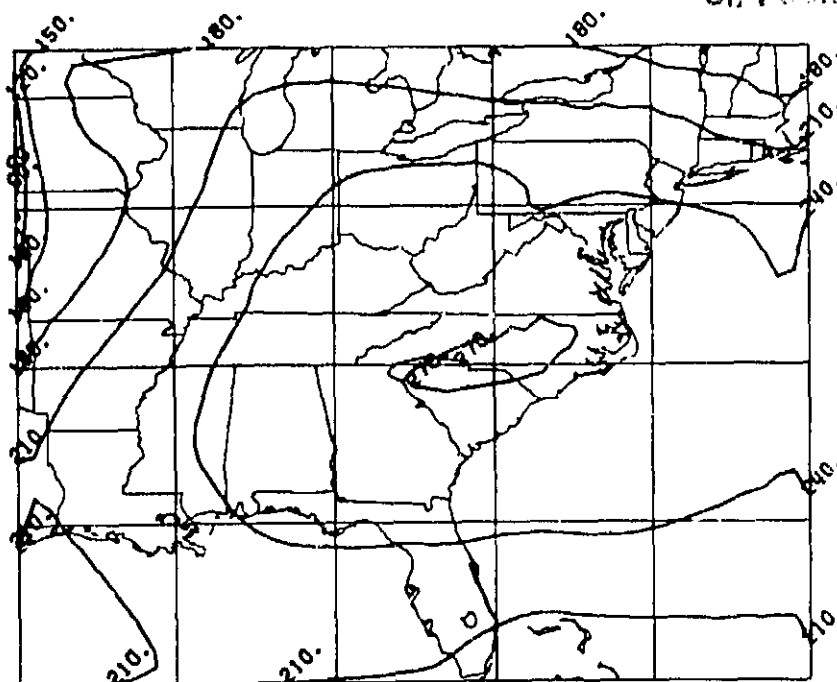


Fig. 35 Twelve-hour forecast 1000 mb height (top) and temperature (bottom) fields for experiment VN valid at 00 GMT, 16 January 1979.

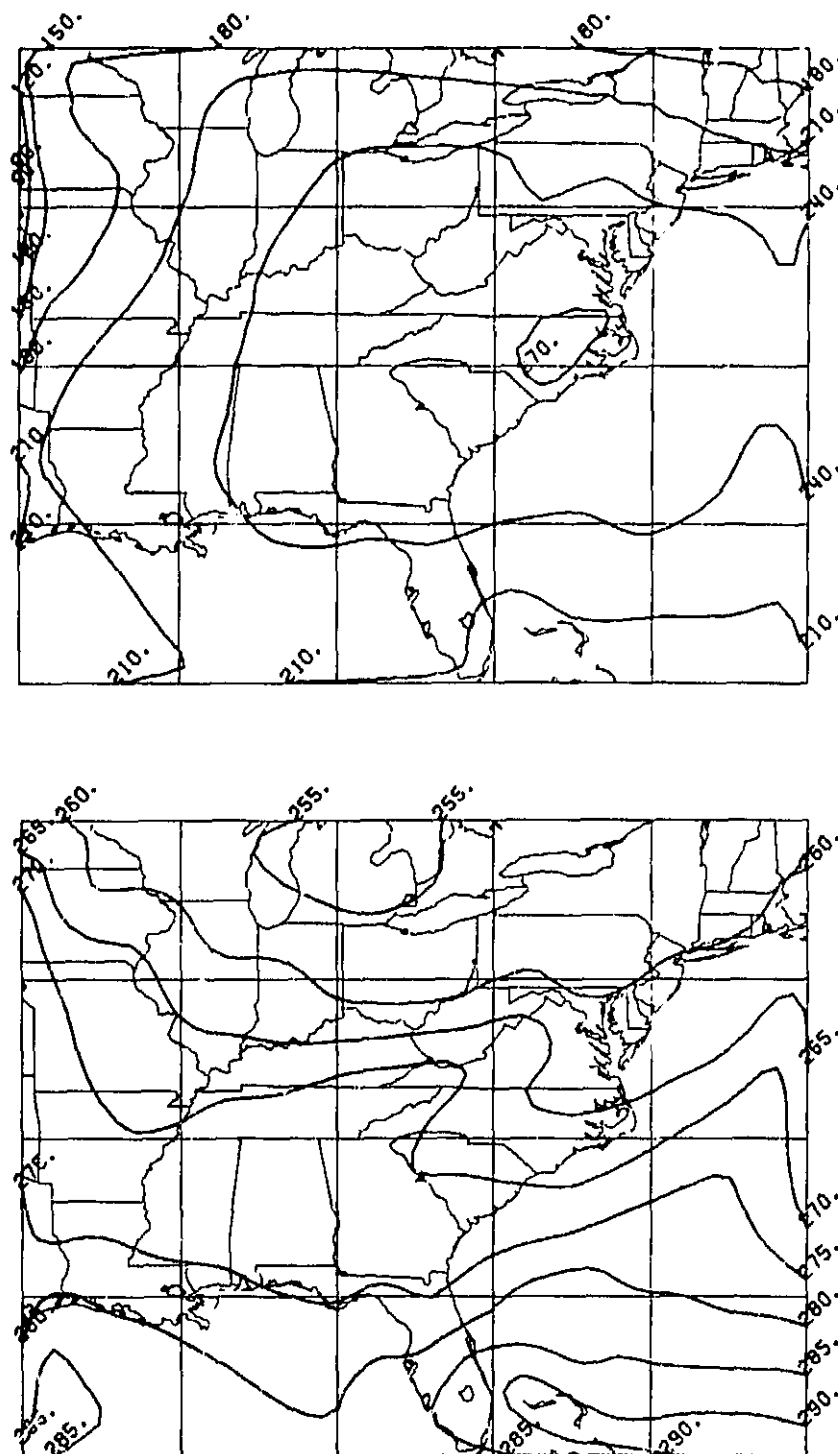


Fig. 36 Twelve-hour forecast 1000 mb height (top) and temperature (bottom) fields for experiment GS valid at 00 GMT, 16 January 1979.



OF POOR QUALITY

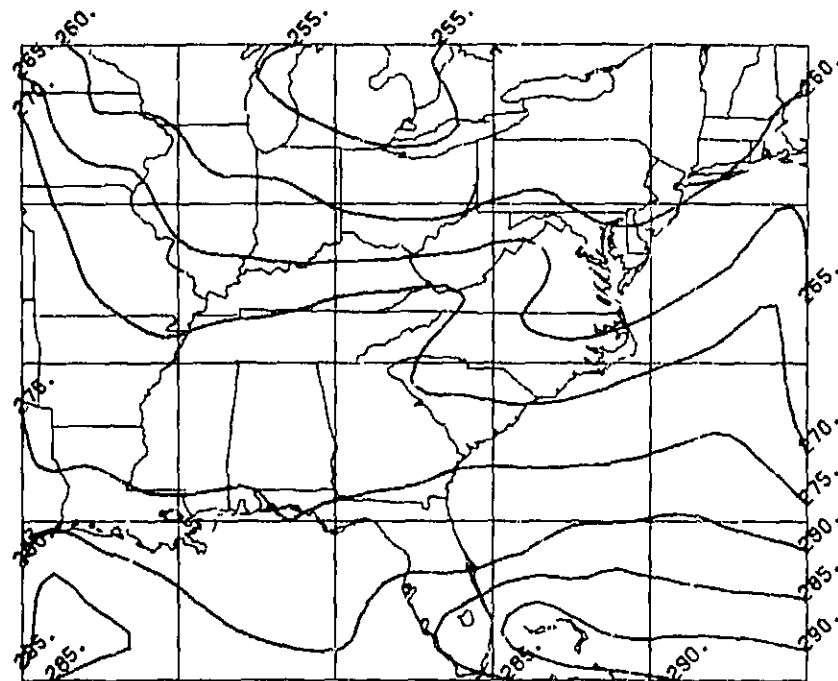
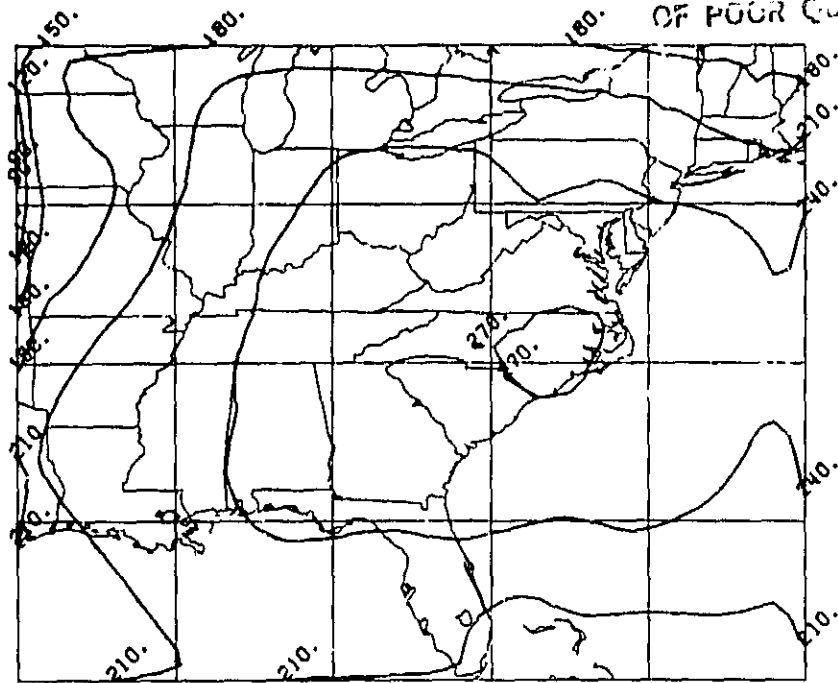


Fig. 37 Twelve-hour forecast 1000 mb height (top) and temperature (bottom) fields for experiment GN valid at 00 GMT, 16 January 1979.

ORIGINAL P. 1  
OF POOR QUALITY

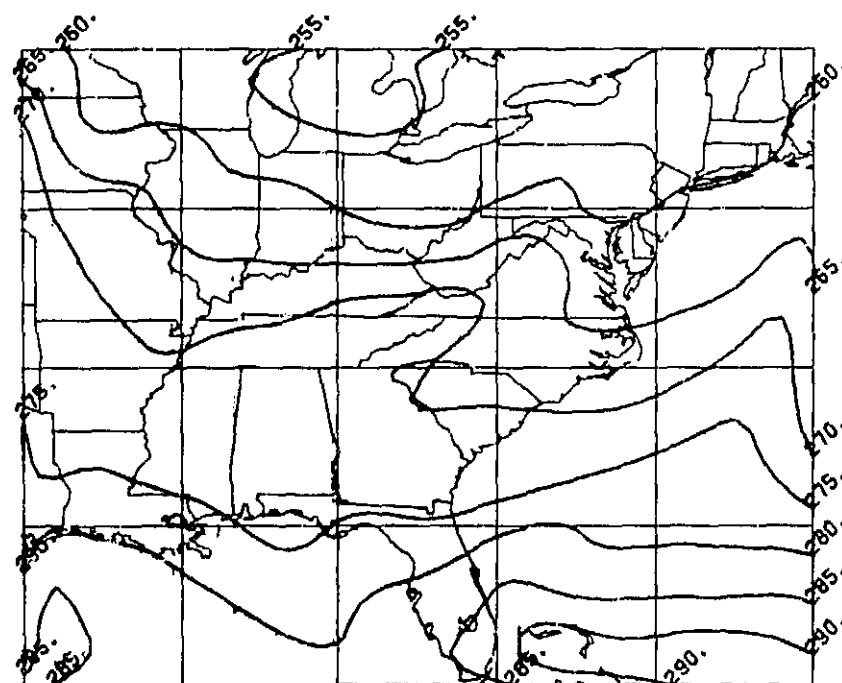
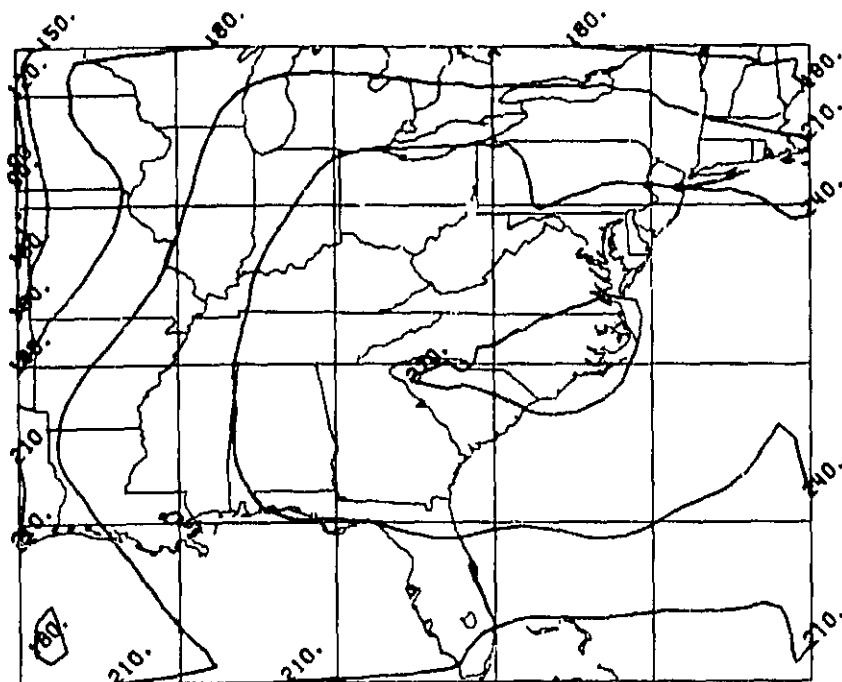


Fig. 38 Twelve-hour forecast 1000 mb height (top) and temperature (bottom) fields for experiment CS valid at 00 GMT, 16 January 1979.

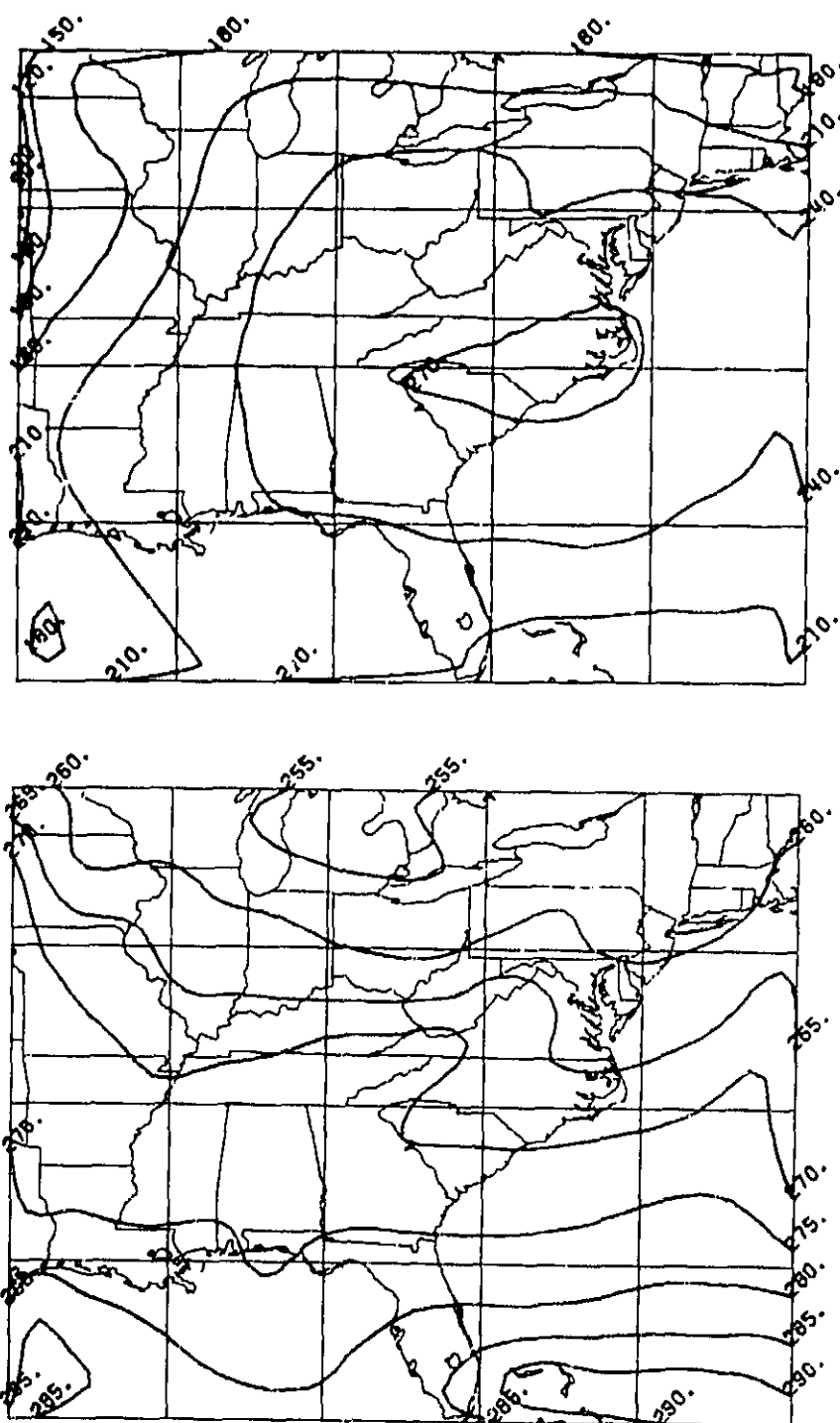


Fig. 39 Twelve-hour forecast 1000 mb height (top) and temperature (bottom) fields for experiment CN valid at 00 GMT, 16 January 1979.

## 850-mb Height Forecast

	12-hour		24-hour	
	RMSE	S1	RMSE	S1
VS	11.5	26.9	10.8	34.8
VN	11.6	26.9	10.9	35.2
CS	11.7	30.8	12.3	38.6
CN	11.7	31.0	12.3	38.8
GS	12.3	32.4	11.9	38.1
GN	12.5	32.2	11.5	38.4

## 500-mb Height Forecast

	12-hour		24-hour	
	RMSE	S1	RMSE	S1
VS	18.4	13.3	22.4	17.3
VN	18.5	13.5	22.4	17.2
CS	17.1	13.3	24.5	18.1
CN	17.0	13.3	24.4	18.0
GS	17.5	13.2	23.6	17.8
GN	17.4	12.9	23.2	17.6

Table 2. Root mean square errors and S1 scores for the forecast experiments.

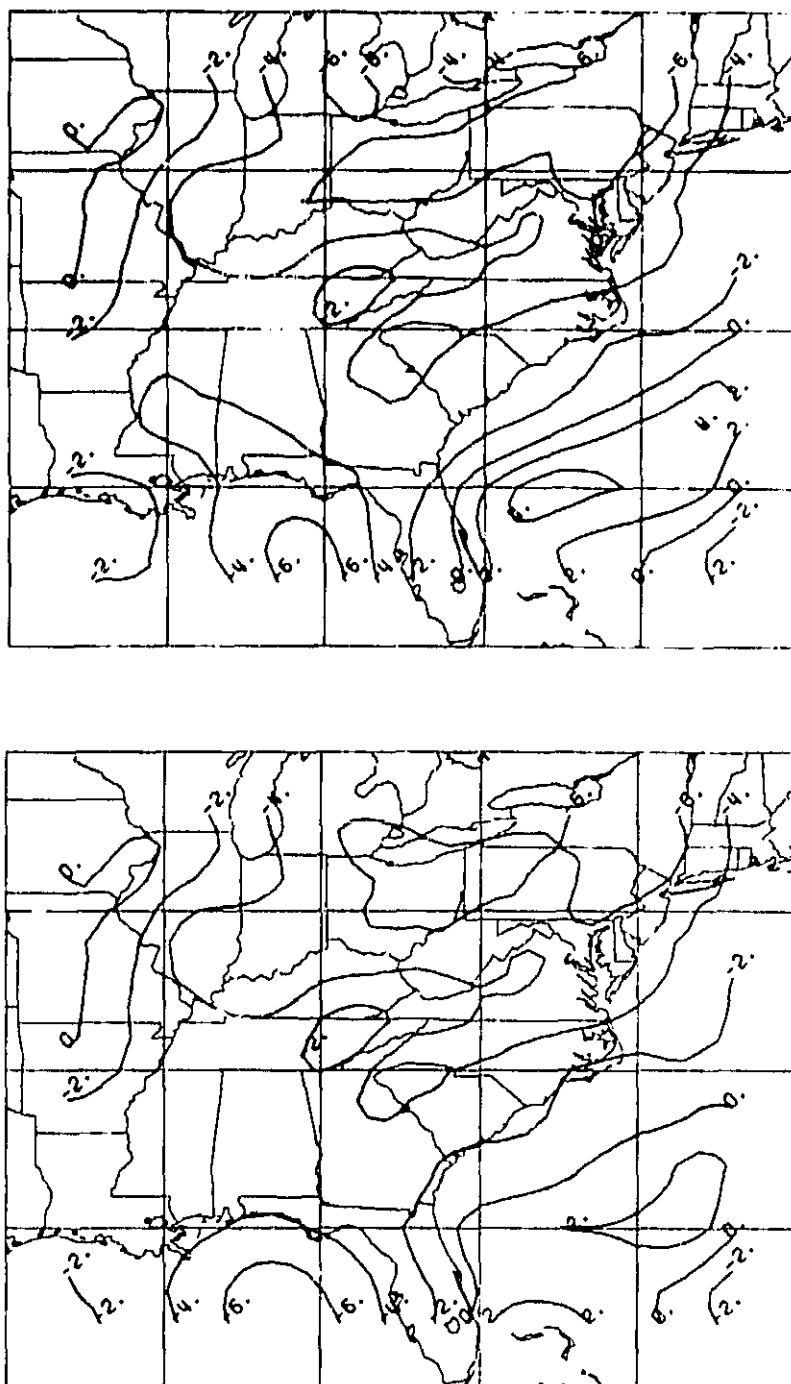


Fig. 40 Difference fields between lowest 12-hour forecast model level temperature and temperatures interpolated from the FGGE Level III-b data set valid at 00 GMT, 16 January 1979, for experiments VS (top) and VN (bottom).

After 24 hours both the RMSE's and SI scores for VS and VN are lower than for the other experiments. At 500 mb there does not appear to be any significant differences among the SI scores or RMSE's for the different experiments although for 24 hours VS and VN appear to have slightly lower values. In no case do we see any indication of improved skill or lowered RMSE's due to assimilation of satellite temperature data. However, due to the limitations of these objective comparisons, this is not surprising. We saw before that the most noticeable effect of assimilation was the enhancement of lower level temperature gradients off the southeast coast. From looking at Fig. 33 we know that this type of temperature gradient will not be reflected in the FGGE Level III-b data and hence the SI scores. Since the upper air stations are predominantly located on the land we cannot expect to see any reflection of this in the RMSE's also.

In order to more closely see the effects of satellite data assimilation we compared the differences between the temperatures for the lowest model level and for the FGGE Level III-b data interpolated to that level. In Fig. 40 we can see these difference fields for the 12-hour VS and VN forecasts valid at 00 GMT, 16 January 1979. Similar results were seen for the other experiments. This figure points out that the only striking difference between these forecasts is the enhanced temperature gradient shown by VS off the southeast coast. This is a significant difference whose impact would not be detected by either of the objective statistical comparison techniques. However, given that the variational temperature analysis scheme produced enhanced low level temperature gradients along the southeast coast, we believe that this figure illustrates that this information has been effectively assimilated into the CMM.

## 6. CONCLUSIONS AND RECOMMENDATIONS

The satellite data available for this study were brightness temperatures from one orbit for the TIROS-N HIRS and MSU channels at 0850 GMT, 15 January 1979. Upon examination of the data we concluded that it contained useful temperature information in cloud-free areas for the very lowest levels of the atmosphere. The data were biased but were found to possess high resolution temperature gradient information. Examination of the FGGE Level II-b and III-b data we had available for that time showed that this was information that could not be obtained from conventional sources.

In order to combine the horizontal temperature gradient information derived at high resolution from satellite with the absolute temperature information obtained from conventional sources, we developed a variational temperature analysis scheme. This scheme was tested upon the data available and was found to be successful at combining the two types of information. Using the scheme we were able to produce temperature fields which possessed the gradient information contained in the satellite observations and at the same time were unbiased and possessed relatively small RMSE's with respect to the conventional observations of temperature.

To test the impact of the satellite data upon mesoscale model forecasts we conducted several forecast experiments utilizing the CIMMS Mesoscale Model. Since the domain of a mesoscale model is typically covered by one pass of a polar-orbiting satellite it was natural to treat the data assimilation problem as an initialization problem. Three different model initialization procedures were tested with and without the use of satellite data. The first was a three-dimensional, multivariate variational objective analysis scheme;

the second was a two-dimensional, univariate Cressman scheme; and the third was identical to the second except that the resulting mass and momentum variables were coupled using a variational static balancing scheme.

First, we examined the initialization procedures' effectiveness at providing balanced fields for the forecast model start-up. Root mean squares of pressure tendency over the model domain were computed each time step as a measure of the initial imbalance and resulting model adjustment for forecasts initialized with each scheme. It was found that the variational scheme and the statically balanced Cressman scheme produced fields which permitted the model forecasts to begin with much less noise than the univariate Cressman scheme. Over the course of the model forecasts it was found that the noise level was less overall when the multivariate, variational procedure was used.

Twenty-four hour forecasts were run for each of the three initialization procedures with and without the use of the low level satellite temperature data. Objective statistical scores (RMSE's from conventional observations and SI scores from FGGE Level III-b fields) were computed and it was found that there was no significant impact upon any of the forecasts due to satellite data assimilation. However, it was found that the forecasts produced using the multivariate, variational initialization procedure were significantly better than those produced using the two Cressman schemes. Subjective examination of the forecast fields revealed, however, that the satellite data assimilation did have an impact but that it could not be measured using conventional observations or analyses derived from conventional observations. All of the assimilation forecasts displayed the advection of the enhanced low-level temperature gradient from the southeast U.S. coast out into the



Atlantic. Unfortunately, this feature, which was the major difference between the assimilation and non-assimilation forecasts, occurred in an area with virtually no observational coverage. These forecasts did show that the satellite-derived temperature information was indeed successfully assimilated into the forecast model.

Based on the results of this study we would make the following recommendations for future research in this area. First, the brightness temperatures from the individual satellite channels were found to be useful only at the lowest levels of the atmosphere and for cloud-free conditions. A study similar to this one should be conducted using the highest horizontal resolution satellite-derived sounding data available from the TIROS-N satellite. The variational temperature analysis procedure was shown to be successful at combining the information obtained from satellite observations with that obtained from conventional observations. The impact of this was lessened, however, by the limitations of the satellite data available. In order to fully test its utility experiments must be conducted using a better collection of satellite observations. Finally, satellite-derived moisture profiles have been found to be similar to temperature profiles in that horizontal gradient patterns have been found to be reasonable and consistent with the meteorological processes involved (Smith, et al., 1981; Hayden et al., 1981). An analysis scheme similar to the variational temperature analysis scheme should be developed and applied to satellite-derived moisture profiles and conventional observations. Forecast experiments similar to those described in this report should then be conducted to assess the impact of satellite moisture assimilation.

# BIBLIOGRAPHY

- Cressman, G., 1959: An Operational Objective Analysis System. **Mon. Wea. Rev.**, 87, 367-374.
- Hayden, C., W. Smith, and H. Woolf, 1981: Determination of Moisture from NOAA Polar Orbiting Satellite Sounding Radiances, **JAM**, 20, 450-466.
- Mesinger, F., and A. Arakawa, 1976: Numerical Methods Used in Atmospheric Models. GARP Publ. Ser. No. 17, Vol.1, 66 pp.
- Miyakoda, K., R. Strickler, and J. Chludzinski, 1978: Initialization with the Data Assimilation Method. **Tellus**, 30, 32-54.
- Perkey, D.J., and C.W. Kreitzberg, 1976: A Time-dependent Lateral Boundary Scheme for Limited-area Primitive Equation Models. **Mon. Wea. Rev.**, 104, 744-755.
- Sasaki, Y., 1976: Variational Design of Finite-difference Schemes for Initial Value Problems with an Integral Invariant. **J. Comput. Phys.**, 21, 270-278.
- \_\_\_\_\_, 1977: Variational Design of Finite-difference Scheme for Initial Value Problems with a Global Divergent Barotropic Model. **Beitr. Phys. Atmos.**, 50, 284-289.
- \_\_\_\_\_, and J. Goerss, 1982: Satellite Data Assimilation Using NASA Data Systems Test 6 Observations. **Mon. Wea. Rev.**, 110, 1635-1644.
- Smith, W., F. Nagle, C. Hayden, and H. Woolf, 1981: Vertical Mass and Moisture Structure from TIROS-N. **BAMS**, 62, 388-393.
- Susskind, J., J. Rosenfield, D. Reister, and M. Chahine, 1982: The GLAS Physical Inversion Method for Analysis of HIRS2/MSU Sounding Data. Nasa Tech. Memo. 84936, 101 pp.
- Teweles, S., and H. Wobus, 1954: Verification of Prognostic Charts. **BAMS**, 35, 455-463.